Calcium carbonate measurements in the surface global ocean based on Moderate-Resolution Imaging Spectroradiometer data

W. M. Balch
Bigelow Laboratory for Ocean Sciences, West Boothbay Harbor, Maine, USA

Howard R. Gordon
Physics Department, University of Miami, Coral Gables, Florida, USA

B. C. Bowler, D. T. Drapeau, and E. S. Booth
Bigelow Laboratory for Ocean Sciences, West Boothbay Harbor, Maine, USA

Received 25 June 2004; revised 7 February 2005; accepted 17 March 2005; published 2 July 2005.

[1] We describe a two-band algorithm for the remote quantification of the ocean's suspended calcium carbonate (also known as particulate inorganic carbon (PIC)), based on normalized water-leaving radiance at 440 and 550 nm. We tested this algorithm using ship-derived and satellite-derived results from a variety of marine environments. From this validation work we calculated the overall accuracy of the satellite-based PIC estimates, assuming different timescales and space scales for binning. After performing the validation work we applied the two-band algorithm to water-leaving radiance data from 2002, sampled by Moderate-Resolution Imaging Spectroradiometer (MODIS)/Terra (a 36-band satellite spectrometer designed to observe land, ocean, and atmosphere), and we derived seasonal, global maps of the standing stock of pelagic PIC as well as particulate organic carbon (POC). These data, along with limited observations on the turnover time of calcium carbonate coccoliths in the euphotic zone, provide some new insights into global rates of pelagic calcite production.

Citation: Balch, W. M., H. R. Gordon, B. C. Bowler, D. T. Drapeau, and E. S. Booth (2005), Calcium carbonate measurements in the surface global ocean based on Moderate-Resolution Imaging Spectroradiometer data, *J. Geophys. Res.*, *110*, C07001, doi:10.1029/2004JC002560.

1. Introduction

1.1. Production and Distribution of Particulate Inorganic Carbon in the Surface Ocean

[2] Particulate inorganic carbon (PIC; or $CaCO_3$) is found throughout the coastal and open oceans of the world and it represents about 1/4 of all marine sediments [*Broecker and Peng*, 1982; *Seibold and Berger*, 1982]. $CaCO_3$ is produced in shallow waters by either coral reefs or macrophytic algae (e.g., *Halimeda*), or in the plankton, by coccolithophores, foraminifera, and pteropods [*Milliman*, 1993]. These plankton eventually fall through the water column, and are deposited in shallow and deep sea sediments. Mineralization of their $CaCO_3$ shells can involve five allotropic modifications, with calcite and aragonite being the most abundant [*Stumm and Morgan*, 1981]. Previous calculations of the inventory of total alkalinity and residence times of various water masses have demonstrated that calcification by oceanic and shelf plankton accounts for ~2/3 of global calcification [*Milliman*, 1993]. The current global $CaCO_3$ production rate is thought to be ~0.6 Gt C as $CaCO_3$ yr^{-1} with ~0.3 Gt C produced in the deep sea [*Milliman*, 1993]. Two other estimates of global calcification in shelf, slope and oceanic waters are ~0.9 Gt C yr^{-1} [*Morse and Mackenzie*, 1990] and ~1.1 Gt C yr^{-1} [*Wollast*, 1994], almost 2 × higher than *Milliman* [1993]. *Wollast* [1994] suggested that sediment trap artifacts or overestimates of dissolution were the cause of lower global calcification estimates. *Milliman et al.* [1999] estimated that pelagic production of calcium carbonate was 0.7 Gt PIC yr^{-1}. This value was closer to the range of deep sea $CaCO_3$ dissolution estimates (0.7–0.9 Gt PIC yr^{-1}) given by *Archer* [1997], but still less than the estimated global $CaCO_3$ rain rate of ~1 Gt PIC yr^{-1} [*Archer and Maier-Reimer*, 1994; *Archer*, 1997]. More recently, *Feely et al.* [2004] used the seasonal cycle of euphotic zone alkalinity to estimate the range of annual calcite production. Their values varied from 0.8–1.4 Gt PIC yr^{-1}.

1.2. Marine $CaCO_3$ Cycle: Biogeochemistry Implications

[3] The burning of fossil fuels appears to have major impact on oceanographic, ecological and physiological conditions [*Sabine et al.*, 2004] through effects (sometimes opposing) on temperature, stratification, pH, etc. [*Bates et al.*, 1996; *Lavrentyev et al.*, 2001; *Peng et al.*, 1998; *Riebesell et al.*, 1993, 2000, 2001; *Stockwell et al.*, 2000]. Nonetheless, it is not yet known whether the net effect of

0148-0227/05/2004JC002560$09.00

increased pCO_2 will shift the ratio of export of particulate organic carbon to particulate inorganic carbon. Such a change could then affect the ability of the ocean to act as a CO_2 sink. It is clear that not enough is known about the calcium carbonate standing stock in the sea to allow unambiguous prediction of its response to different forcing.

[4] Anthropogenic CO_2 can be neutralized by reactions with marine calcium carbonate via the dissolution reaction

$$CO_2 + CaCO_3 + H_2O = 2HCO_3^- + Ca^{2+}. \quad (1)$$

As the oceans become enriched in fossil fuel-derived CO_2, the locations and extent of dissolution will increase as a function of changes in the $CaCO_3$ saturation state. *Feely et al.* [2004] estimated that the depths of calcite and aragonite saturation have shoaled as much as several hundred meters since the beginning of the industrial revolution, due to the ventilation of anthropogenic CO_2 into the sea. On longer timescales, variations in calcium carbonate cycling have been proposed to account for a significant fraction of the ~80 ppm increase in atmospheric CO_2 from glacial to interglacial times [*Archer and Maier-Reimer*, 1994; *Boyle*, 1988; *Broecker and Peng*, 1989]. Even on thousand year timescales, sedimentary $CaCO_3$ is a major buffer of atmospheric CO_2 [*Archer et al.*, 1998; *Broecker and Takahashi*, 1977; *Sundquist*, 1993]. Surface production and deep dissolution of $CaCO_3$, the ocean "carbonate pump," has the effect of raising atmospheric pCO_2 by roughly 25 ppm [*Maier-Reimer*, 1996; *Najjar et al.*, 1992; *Volk and Hoffert*, 1985], with local surface ocean impacts as high as 50 ppm in coccolithophore blooms [*Holligan et al.*, 1983; *Robertson et al.*, 1994]. Thus even on short timescales, changes in the carbonate standing stocks could be significant to atmospheric CO_2 budgets.

[5] Knowledge of the global distribution of calcium carbonate may help explain significant anomalies in alkalinity that can be found in the surface ocean, which ultimately result from variability in calcification and dissolution. While calcium carbonate is generally oversaturated in the surface ocean (as much as 5 times), significant negative Ca^{++} anomalies can be seen in the top 200 m presumably due to net calcification and subsequent sinking of the $CaCO_3$. In slightly deeper waters (while still above the lysoclines for aragonite and calcite), there are well-documented positive anomalies in Ca^{++}, suggesting net calcite dissolution [*Milliman et al.*, 1999]. Taken together with sediment trap measurements, it appears that at least half of the surface-produced calcium carbonate must dissolve shallower than 1000 m to be consistent with sediment trap fluxes at that depth [*Balch et al.*, 2000; *Balch and Kilpatrick*, 1996; *Feely et al.*, 2004; *Troy et al.*, 1997].

1.3. Case for Using Remote Sensing to Study the Calcium Carbonate Cycle

[6] Clearly, the ability to remotely map suspended $CaCO_3$ from space would provide new insights into the global carbonate cycle. In addition to its impact on atmospheric CO_2 on a variety of timescales, there are several reasons for using remote sensing to study suspended $CaCO_3$. The first reason is the impact of $CaCO_3$ producers on the upper ocean light field, especially during coccolithophore bloom events [*Ackleson et al.*, 1988; *Balch et al.*, 1989; *Holligan et al.*, 1993, 1983; *Tyrell et al.*, 1999]. In typical nonbloom situations, backscattering of light by suspended coccoliths routinely accounts for 10–20% of all visible backscattered light from the sea [*Balch et al.*, 1999]. This percentage can exceed 90% in coccolithophore blooms [*Balch et al.*, 1991] when the concentration of calcite is much higher. The second reason for using remote sensing to study the global distribution of $CaCO_3$ is that $CaCO_3$ producers are well known for the production of dimethylsulfide (DMS) which has links to planetary albedo [*Charlson et al.*, 1987; *Shaw*, 1983]. One coccolithophore species, *Emiliania huxleyi*, is a significant producer of dimethylsufide [*Keller et al.*, 1989; *Malin et al.*, 1993; *Matrai and Keller*, 1993]. A third reason for remotely studying the global marine $CaCO_3$ distribution is that our interpretation of the paleorecord in marine sediments hinges on what we know about the production and dissolution of $CaCO_3$ in the modern ocean. Understanding extant global distributions of PIC can aid in understanding paleopatterns of PIC deposition. Lastly, $CaCO_3$ serves as ballast for particulate organic matter, especially in the deep sea, where the relative abundance of $CaCO_3$ in particulate material becomes dominant. Recent work [*Armstrong et al.*, 2002; *Francois et al.*, 2002; *Iglesias-Rodrigues et al.*, 2001] has focused on the dominant role of ballast minerals such as calcium carbonate as a carrier of organic carbon into the ocean interior. Understanding global PIC distributions through remote sensing will eventually allow better calculation of global export fluxes of carbon.

1.4. Optical Properties and Carbon Content of Coccoliths: The Heart of the Optical Algorithm

[7] Given the importance of suspended calcium carbonate to the global carbon cycle, a remote means to detect it is essential. Unlike phytoplankton pigments, which, when present, decrease the radiance in the blue but increase it only slightly in the green, coccolithophores increase the radiance uniformly in both the blue and green [*Gordon et al.*, 1988]. Thus their remote study requires an understanding of the actual water-leaving radiance rather than just radiance ratios as in the case of pigments [*Gordon and Morel*, 1983]. Furthermore, the "flattening" of the reflectance spectrum in coccolithophore blooms implies that the standard ratio pigment algorithms [*Gordon and Morel*, 1983] will not provide correct pigment retrievals within the blooms [*Balch et al.*, 1989]. A previous solution to this problem was to use a coccolithophore "flag" to check for regions of high coccolithophore abundance, whereupon the associated pigment concentrations could be flagged as suspect [*Brown and Yoder*, 1994].

[8] A fundamentally different remote sensing approach for the remote sensing of coccolithophores is to use individual water-leaving radiance values, not ratios, to resolve the interacting effects of coccolithophore calcite and chlorophyll in seawater. *Gordon et al.* [1988] developed a prototype model for explaining the dependence of the water-leaving radiance on the concentration of constituents in Case 1 waters. Briefly, the normalized water-leaving radiance is related to the absorption and scattering properties of the biogenic components of the water, phytoplankton and their associated detritus. This model provides the basis for extraction of the concentration of the

detached coccoliths, or the coccolith PIC concentration, based on water-leaving radiance measurements and known optical properties of calcium carbonate.

[9] The calcite-specific backscattering cross section for coccolithophores is critical to the above optical PIC algorithm. This has been previously determined to be about 1.37 m^2 mol PIC^{-1}, based on lab and field studies [*Balch et al.*, 1999]. Obviously, this property is related to the size, shape and mass of the calcite coccoliths [*Gordon and Du*, 2001]. It is important to point out that even within the species *E. huxleyi*, there can be variability in the PIC content of coccoliths, especially when comparing results from culture and field measurements [*Paasche*, 2002]. Such variance will invariably affect the coccolith- and PIC-specific backscattering cross sections, and, in turn, the accuracy of any optically derived PIC estimates. This variance exists because of assumptions about the numbers of coccoliths attached to each coccolithophore as well as effects of growth conditions on coccolith production. For example, PIC content per *E. huxleyi* coccolith has been estimated in many studies: 0.16 pg [*Paasche*, 1962], 0.45–0.5 pg for field measurements from a NE Atlantic bloom [*Holligan et al.*, 1983], 0.2 pg for measurements of a Gulf of Maine bloom (see *Balch* [1991], but note correction [*Balch*, 1991]), 0.26 pg based on both field and culture measurements [*Balch et al.*, 1992], 0.21 pg (P. M. Holligan, unpublished calcite measurements for the NE Atlantic bloom measurements as cited by *Balch et al.* [1992]), 0.47–1.05 pg for measurements from a North Atlantic bloom [*Balch et al.*, 1996a; *Fernández et al.*, 1993].

[10] The above observations suggest that field measurements of coccolith carbon content often are greater than measurements from cultures. Results from nonbloom measurements in the Equatorial Pacific [*Balch and Kilpatrick*, 1996] and Arabian Sea [*Balch et al.*, 2000] certainly support this contention, as do observations of *Paasche* [2002]). We surmise that PIC present in other relatively rare, undocumented, calcite particles (e.g., other rare coccolithophores, foraminifera, and pteropod species, resuspended calcite particles or even fecal pellets containing coccoliths [*Keller et al.*, 1992]) contribute to the elevated PIC coccolith content measured in the field.

[11] More recent culture-based estimates of PIC per coccolith for *E. huxleyi* (based on Ca measurements from cell-free suspension) have shown values of about 0.2 pg PIC, consistent with previous culture measurements: 0.18–0.25 pg PIC for an Atlantic clone [*Paasche*, 1998, 1999], 0.20–0.23 pg for a clone from coastal Scandinavia [*Paasche*, 1999; *Paasche et al.*, 1996], 0.27 pg for a Mediterranean clone [*Paasche*, 1999]. X-ray analysis of individual coccoliths showed 0.201 pg PIC per coccolith [*Fagerbakke et al.*, 1994]. The above cell-free PIC estimates are reasonably close to the theoretical value of 0.276 pg estimated by *Young and Ziveri* [1999] using coccolith dimensions.

[12] These observations suggest that the overall strategy for designing a radiance-based PIC algorithm clearly should be to incorporate the light scattering properties of *E. huxleyi*, consistent with (1) its large numerical abundance in the global ocean (including frequent mesoscale blooms) and (2) its relatively stable PIC coccolith content and an optical backscattering cross section for *E. huxleyi*–sized coccoliths that is orders of magnitude greater than for larger calcite-containing particles in the sea, such as foraminifera and pteropods [*Balch et al.*, 1996a]. This means that the bulk of calcite-related reflectance likely originates from small, *E. huxleyi*–sized coccoliths, not larger (and much less abundant) foraminfera and pteropods. While most historical literature supports a value of ~0.2 pg PIC per coccolith to convert coccolith concentration to PIC, it is likely that algorithm PIC estimates based on this conversion may be underestimates of the total PIC concentration since they nonetheless neglect rare, relatively large, suspended calcite particles.

[13] In this paper, we present a formalized description of a two-band algorithm for the determination of the concentrations of detached coccoliths, suspended calcium carbonate and chlorophyll based on normalized water-leaving radiance at 440 and 550 nm. We present validation results for this optical algorithm based on shipboard measurements from a variety of environments. Next we calculate the overall accuracy of the satellite-based PIC estimates, assuming different time and space binning. We apply the two-band algorithm to water-leaving radiance data from MODIS/Terra (a 36-band satellite spectrometer designed to observe land, ocean and atmosphere) to produce global PIC maps. Last, we make some preliminary inferences about the expected global rates of calcite production based on limited observations from a few ocean regions of the turnover time of calcite coccoliths in the euphotic zone.

2. Methods

[14] As described below, the two-band PIC algorithm is based on a semianalytic model of ocean color developed by *Gordon et al.* [1988] to explain the variation of water-leaving radiance with pigment concentration observed in radiance measurements of *Clark* [1981]. (Note that the pigment concentration (C) is defined as the sum of the concentrations of chlorophyll *a* and phaeophytin *a* measured fluorometrically.)

[15] Field validation measurements used to test this algorithm were made in the Straits of Florida, Arabian Sea, North Atlantic (south of Iceland), and Gulf of Maine. We also include measurements associated with an experimental addition of Cretaceous chalk to surface seawater in the NW Atlantic (dubbed "Chalk-Ex," complete details to be published elsewhere). Most of the data, in fact, come from the Gulf of Maine, due to the proclivity of naturally occurring coccolithophore blooms in the region as well as the presence of our long-term sampling program aboard a passenger ferry, the M/S *Scotia Prince* [*Balch*, 2001; *Balch et al.*, 2004].

[16] Shipboard validation consisted of parallel measurements of acid-labile backscattering (b'_b) with a multiangle light-scattering photometer [*Balch et al.*, 2000, 2001; *Balch and Drapeau*, 2004; *Balch et al.*, 1999, 1996a] and PIC determinations [*Balch et al.*, 1996a; *Balch and Kilpatrick*, 1996; *Fernández et al.*, 1993] on sea water samples. We also validated the algorithm using measurements of upwelling radiance, sky radiance and downwelling irradiance at 443 and 555 nm, made with a Satlantic SAS system mounted on the above-mentioned ferry, using protocols

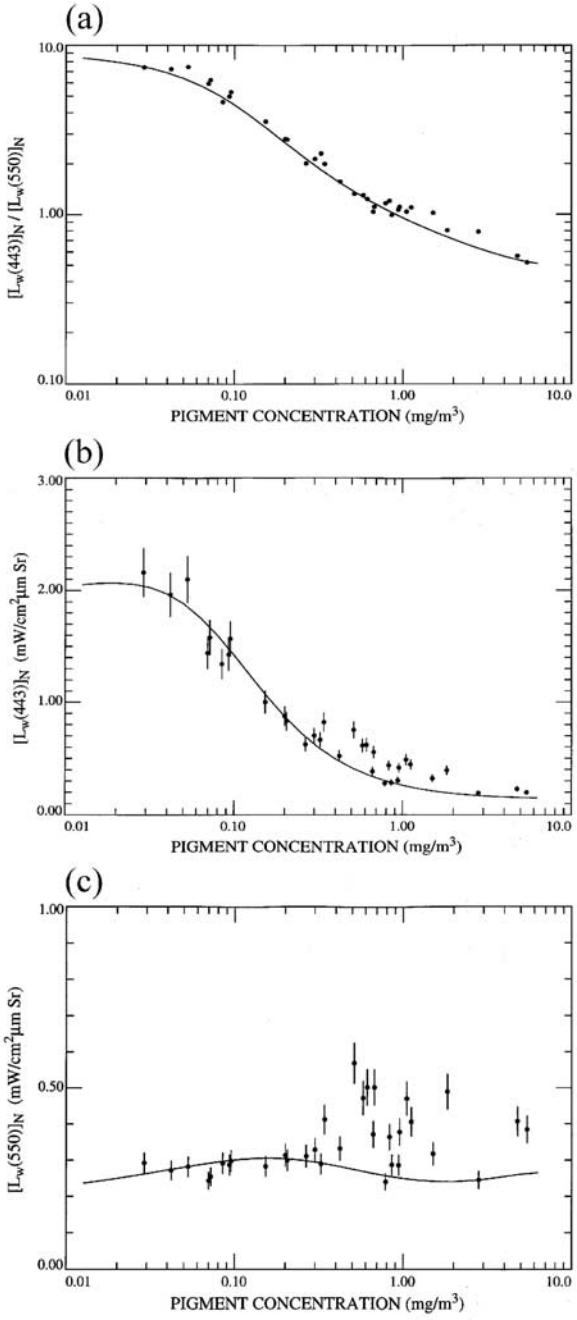

Figure 1. (a) Normalized water-leaving radiance ratio between 443 and 550 nm as a function of the pigment concentration. (b) Normalized water-leaving radiance at 443 nm as a function of the pigment concentration. (c) Normalized water-leaving radiance at 550 nm as a function of the pigment concentration. Data points are from *Clark* [1981], and the curve is the result of the semianalytic model [*Gordon et al.*, 1988]. The plankton-detritus scattering parameter in the model has been adjusted to provide the best fit to the *Clark* [1981] data for concentrations less than 0.3 mg m^{-3}.

described by *Mueller et al.* [2003]. Briefly, the location of the radiance sensors on the bow of the ferry avoided any potential wake contamination in the upwelling radiance data. The upwelling (ocean) and downwelling (sky) radiance sensors were always pointed 40° from nadir and zenith, respectively, and 90°–120° from the Sun's azimuth to minimize Sun glint. A downwelling irradiance sensor was located on the uppermost deck of the ship, away from any of the ship's superstructure, in order to achieve a full view of the sky. All data were sampled at 16 Hz and only the lowest 5% of the data were used, in order to eliminate highly reflective white caps. SAS-based PIC estimates are reported only if made under clear-sky conditions.

[17] MODIS/Terra data used in the validation activities were sampled at 1 km resolution. Data for global images were used at 36 km resolution. Version 4.1 of the MODIS processing software was used to process the data. MODIS processed data are assigned a product quality level ranging from 0 (best) to 3 (worst). The quality of the MODIS level 2 products for the coccolith concentration, the PIC concentration and pigment concentration in the presence of coccoliths, depend directly on the quality of the input data (normalized water-leaving radiance at 443 nm and 551 nm). Therefore these three products have been assigned the quality level of the input data. Moreover, if the calculated PIC concentration was $\leq$0 or >1000 mg PIC m^{-3} (exceeding the highest level ever observed in a bloom) then the quality level for the coccolith/PIC products and coccolithophore pigment concentration was assigned a quality level of 3 (worst). For the results reported here, we required that the input data, as well as the resultant calcite products, all had quality flags set to zero (highest quality).

3. Results

3.1. Moderate-Resolution Imaging Spectroradiometer (MODIS) Two-Band Algorithm for Coccoliths and Suspended Calcite

[18] Using the data of *Clark* [1981], the *Gordon et al.* [1988] semianalytic radiance model successfully explained the dependence of the blue-green water-leaving radiance ratio on the pigment concentration (Figure 1a). It actually fits the ratio data better over the full range of pigment concentration than the power law fits usually used in the analysis of remotely sensed ocean color data [e.g., see *Gordon and Morel*, 1983]. It was also moderately successful at relating the actual radiances themselves to the pigment concentration. Figures 1b and 1c compare the computed and observed relationship between $[L_w(443)]_N$, $[L_w(550)]_N$ and pigment concentration (C) for the same data shown in Figure 1a. In the figures, the plankton-detritus scattering parameter was adjusted to provide the best fit for $C <$ 0.3 mg m^{-3}. The resulting value of this parameter was well within the range generally found for Case 1 waters [*Gordon and Morel*, 1983]. Also, the "noise" in the relationship for $C >$ 0.3 mg m^{-3} appears to be due to the natural variation in the backscattering of plankton and detritus, as it is consistent with the noise observed in the scattering-chlorophyll relationship for Case 1 waters [*Gordon and Morel*, 1983]. It was straightforward to introduce detached coccoliths from coccolithophores into the model by simply including their contribution to the backscattering.

[19] By direct measurement of detached coccoliths in the Gulf of Maine, *Balch et al.* [1991] showed that at 436

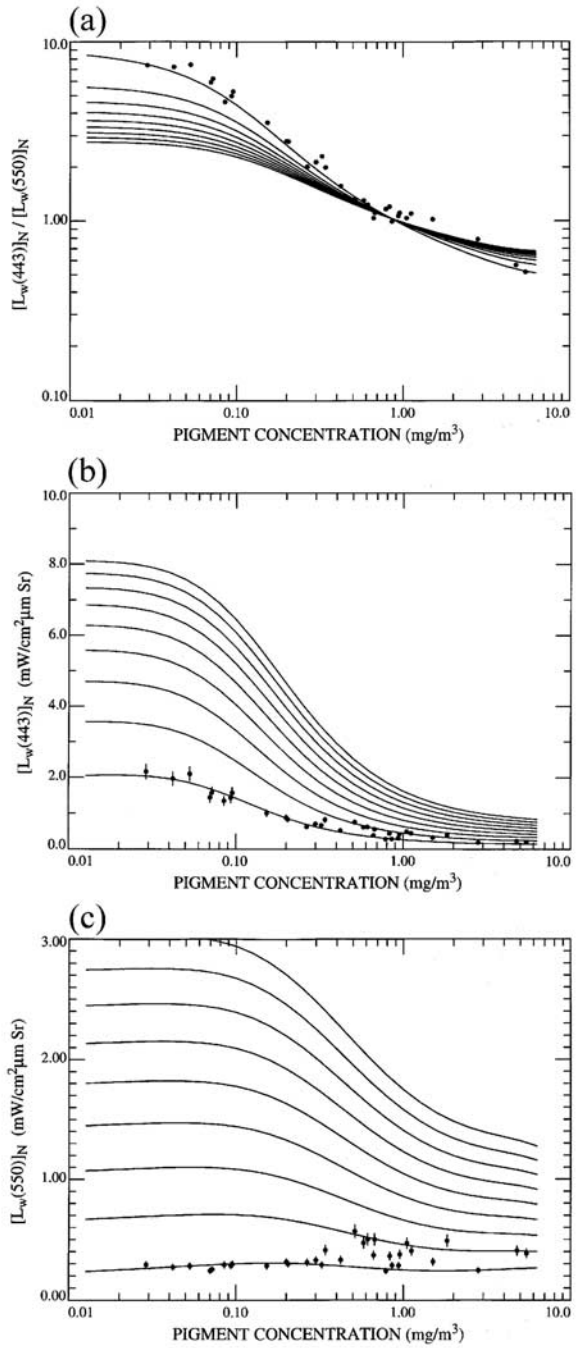

Figure 2. Results of the semianalytic model [*Gordon et al.*, 1988] with increasing coccolith concentration (C_{cc}), plotted along with data points from *Clark* [1981]. (a) Normalized water-leaving radiance ratio between 443 and 550 nm as a function of the pigment concentration. Curved lines are for different values of C_{cc}, increasing from 0 to 200×10^6 coccoliths L^{-1}, in steps of 25×10^6 coccoliths L^{-1} (the higher coccolith concentrations yield the "flatter" curves). (b) Normalized water-leaving radiance at 443 nm as a function of the pigment concentration. (c) Normalized water-leaving radiance at 550 nm as a function of the pigment concentration. For both Figures 2b and 2c, curved lines are for different values of C_{cc} from 0 to 200×10^6 coccoliths L^{-1}, increasing in steps of 25×10^6 coccoliths L^{-1}, from bottom to top.

and 546 nm the backscattering coefficient, $b_b(\lambda)$, of the detached coccoliths was approximated by

$$b_b(\lambda) = A(\lambda)C_{cc}, \tag{2}$$

where C_{cc} was the concentration of detached coccoliths, $A(436) = 1.5 \times 10^{-13}$ m^2 coccolith^{-1}, and $A(546) = 1.1 \times 10^{-13}$ m^2 coccolith^{-1}. On the basis of these measurements the spectral variation of $b_b(\lambda)$ was best described by equation (3):

$$b_b \propto \lambda^{-1.35}. \tag{3}$$

Figures 2a–2c provide the radiance ratio, $[L_w(443)]_N/[L_w(550)]_N$ as functions of C and C_{cc}, as derived from the radiance model. Figure 2a shows that if the blue-green ratio were applied to ocean color data without regard for the presence of coccoliths considerable error would be present in the retrieved pigment concentration. For example, if the measured ratio was 4 and C_{cc} was 75×10^6 coccoliths L^{-1}, C would be approximately 0.05 mg m^{-3} but if coccoliths were ignored, the retrieved value of C would be closer to 0.11 mg m^{-3}. Examination of Figures 2b and 2c shows that, while the coccolith concentration exerts a strong influence on both $[L_w(443)]_N$, C still has a large influence on $[L_w(443)]_N$ but only a moderate influence on $[L_w(550)]_N$. This suggests that it should be possible to separate, with reasonable accuracy, C and C_{CC} in measurements of $[L_w(443)]_N$ and $[L_w(550)]_N$. The two-band algorithm simply consists of inverting the semianalytic model to derive C and C_{cc} from measurements of $[L_w(443)]_N$ and $[L_w(550)]_N$. This is accomplished with the aid of a lookup table that is graphically represented in Figure 3. Examination of Figure 2b suggests that the natural variation in phytoplankton backscattering for $C < 10$ mg m^{-3} corresponds to 0 to 25×10^6 coccoliths L^{-1}. Thus given accurate values of $[L_w(\lambda)]_N$ there will always be an uncertainty in C_{cc} of at least 25×10^6 coccoliths L^{-1}. Figure 3 suggests that the sensitivity of the radiances to C_{cc} falls by about a factor of 2 from low to high C. Note, Figure 3 provides a simultaneous method for deriving both C_{cc} (or the equivalent PIC concentration assuming the coccoliths are from *E. huxleyi*) and C in coccolithophore blooms; however, the sensitivity when the pigment concentration is >2 mg m^{-3} is poor.

3.2. Influence of Atmospheric Correction on the Accuracy of the Two-Band Algorithm

[20] As the two-band PIC algorithm uses absolute values of the water-leaving radiances, it is more susceptible to error in atmospheric correction than algorithms employing radiance ratios. Thus atmospheric correction could be an important source of error, over and above the inherent error in the algorithm due to natural variability in calcite particles in the sea. The atmospheric correction algorithm [*Gordon and Wang*, 1994; *Gordon*, 1997] uses near infrared (NIR) spectral bands to assess the atmospheric interference based on the observation that $[L_w(\lambda)]_N$ is usually negligibly small in the NIR. The algorithm has an inherent error of ±0.002 and ±0.0005 in normalized water-leaving reflectance at 443 and 550 nm, respectively. (Normalized water-leaving reflectance $[\rho_w(\lambda)]_N$ is related

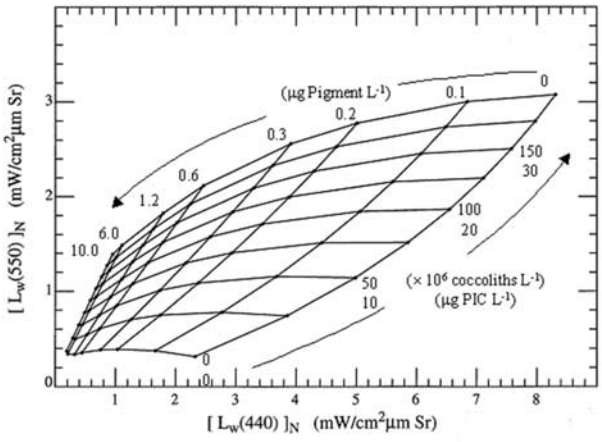

Figure 3. Graphic representation of the lookup table used to estimate the coccolith concentration and the pigment concentration from $[L_w(443)]_N$ and $[L_w(550)]_N$. The lines with the steeper slopes are lines of constant pigment concentration specified in units of μg pigment L^{-1} (written along the top curve on the figure). The lines with more gentle slopes are lines of constant coccolith concentration. The concentration is written along the rightmost curve of constant pigment either in units of 10^6 coccoliths L^{-1} (upper numbers) or after conversion to particulate inorganic carbon (PIC) in units of μg PIC L^{-1} (lower numbers). The natural variability of phytoplankton-detritus backscattering approximately corresponds to the separation between adjacent C_{cc} isopleths.

to $[L_w(\lambda)]_N$ through $[\rho_w(\lambda)]_N = \pi[L_w(\lambda)]_N/F_0(\lambda)$, where F_0 is the extraterrestrial solar irradiance.) However, with increasing coccolith concentration, there will be a non-negligible $[L_w(\lambda)]_N$ in the NIR, and this will lead to additional error in atmospheric correction: the NIR $[L_w(\lambda)]_N$ will be interpreted by the algorithm as a contribution from the atmosphere. Thus we examine the influence of atmospheric correction errors for both low (negligible $[L_w(\lambda)]_N$ in the NIR) and high (significant $[L_w(\lambda)]_N$ in the NIR) coccolith concentrations.

[21] For low coccolith concentrations and the Sun near the zenith, the errors in atmospheric correction described above correspond to uncertainties of ±0.12 and ±0.03 mW cm^{-2} m^{-1} Sr^{-1} in $[L_w(\lambda)]_N$ at 443 and 550, respectively. It should be noted that by the nature of the atmospheric correction algorithm, these errors will have the same sign, i.e., both will be positive or negative. For a coccolith concentration of 15×10^6 coccoliths L^{-1}, the error in C_{cc} will be approximately $\pm 2 \times 10^6$ coccoliths L^{-1} for C near 0.2 mg m^{-3} and approximately $\pm 1 \times 10^6$ coccoliths L^{-1} for C near 1 mg m^{-3}. Thus for low C_{cc} the atmospheric correction–induced error in C_{cc} is negligible compared to that induced by the natural variability in plankton-detritus backscattering. The error induced in C however, is quite large for $C >$ about 1 mg m^{-3}.

[22] To assess the influence of atmospheric correction errors at high C_{cc}, we need to estimate $[\rho_w(\lambda)]_N$ in the NIR. As the absorption coefficient of water is very large in the NIR, the pigment concentration is almost irrelevant in predicting the reflectance, so $[\rho_w(\lambda)]_N \cong b_b(\lambda)/6a_w(\lambda)$,

Table 1a. Error in Retrieved $[L_w(\lambda)]_N$ Due to Coccolith-Induced Water-Leaving Reflectance in the Near-Infrared (NIR)

C_{cc}, coccoliths L^{-1}	$\Delta[L_w(443)]_N$, mW/cm²μ Sr	$\Delta[L_w(550)]_N$, mW/cm²μ Sr
100×10^6	−0.066	−0.057
200×10^6	−0.155	−0.115

where $a_w(\lambda)$ is the absorption coefficient of water. For $C_{cc} = 100 \times 10^6$ coccoliths L^{-1}, this gives $[\rho_w(765)]_N \cong 0.00045$, and $[\rho_w(865)]_N \cong 0.00022$, and doubling C_{cc} will simply double these values. These reflectances will be interpreted by the correction algorithm as an addition to the reflectance of aerosols $\rho_A(\lambda)$. Typical values of $\rho_A(\lambda)$ in a clean maritime atmosphere are ~0.01 with little dependence on wavelength. The correction algorithm uses the aerosol reflectances at 765 and 865 nm to assess the spectral variation $\rho_A(\lambda)$ in the NIR and then uses aerosol models to extrapolate this into the visible. Following the approximate single scattering development provided by *Gordon* [1997], $\rho_A(\lambda) = \exp[a\ (865 - \lambda)]\ \rho_A(865)$, where the parameter a is found by setting λ to 765 nm. Adding the NIR reflectance contribution from the coccoliths to the true $\rho_A(\lambda)$ for a clean maritime atmosphere, i.e., 0.01, determining the apparent a, and computing the apparent $\rho_A(443)$ and $\rho_A(550)$, we arrive at the error in $[L_w(443)]_N$ and $[L_w(443)]_N$ provided in Table 1a. The error induced in the retrieved C_{cc} by the coccolith-induced NIR water-leaving reflectance can be determined by picking a point (C_{cc},C) on Figure 3, adding $\Delta[L_w(443)]_N$ and $\Delta[L_w(550)]_N$ to the normalized water-leaving radiances at the point and determining the change in C_{cc} and C. The resulting change in C_{cc} for both low and high pigment concentration is provided in Table 1b. This suggests that the error induced by NIR coccolith reflectance is also negligible compared to the natural variability in plankton-detritus scattering.

3.3. Validation Results

[23] When ship and satellite validation data were plotted using log axes (which highlights errors at low PIC concentration (Figure 4a)) and linear axes (which better shows the high PIC concentration results from blooms (Figure 4b)), the statistics showed an overall RMS error of 28 μgPIC L^{-1} for 1 kilometer pixel data on any given day. It was possible that the variance about the lines in Figures 4a and 4b, particularly at low PIC concentrations, arose from other non-PIC, nonorganic particles such as biogenic silica. Using only the satellite-derived validation data plotted (i.e., not including ship radiance data), the RMS error was reduced by about a factor of two (to ~15 μgPIC L^{-1} (Figure 4c)). This may indicate that the satellite-derived radiances are more accurate than the ship-derived radiances (which might

Table 1b. Error in Retrieved C_{cc} Due to Coccolith-Induced Water-Leaving Reflectance in the NIR

C, mg/m³	C_{cc}, coccoliths L^{-1}	ΔC_{cc}, %
0.07	100×10^6	−4.2
1.2	100×10^6	−6.4
0.07	200×10^6	−5.3
1.4	200×10^6	−5.4

be expected, given errors in azimuthal and nadir viewing geometries due to ship roll). The causes of the above RMS error may have resulted from a mismatch in the background, noncalcite, b_b value assumed in the algorithm versus that present in the field. For example, it can be seen in the 2002 Gulf of Maine bloom satellite results (designated with open circles in Figure 4c) retrievals where the satellite-derived PIC values approached zero while the ship-derived values were about 30 ug C L^{-1}. Such "blank" bias varied for the other field data sets in Figure 4c, with data falling above and below the 1:1 regression line. Another potential source of variability between ship and satellite measurements might have been due to errors in atmospheric correction.

[24] Even with the increased accuracy associated with using just the satellite-derived PIC estimate, it is difficult using 1 km daily data to accurately derive background oceanic PIC concentrations from satellite since the average global PIC concentration is ~2 μgPIC L^{-1}, less than the RMS error about the line in Figure 4c.

[25] The solution to the above problem, that the background PIC concentration is less than the standard deviation of the technique used to measure it, is to bin the satellite data in space and time, the sample size could be made sufficiently large that the standard errors were then significantly reduced. This is shown in the table of standard errors for the PIC algorithm (Table 2) where, at spatial scales of 4.6 km and time binning of 8 days, the standard errors of the PIC estimates were ~1.2 μgPIC L^{-1}, slightly less than the average global PIC concentration. For data binned over 36 km and 30 days, the standard error was 0.08 μgPIC L^{-1}, 1/16 of the average PIC concentration in the global ocean.

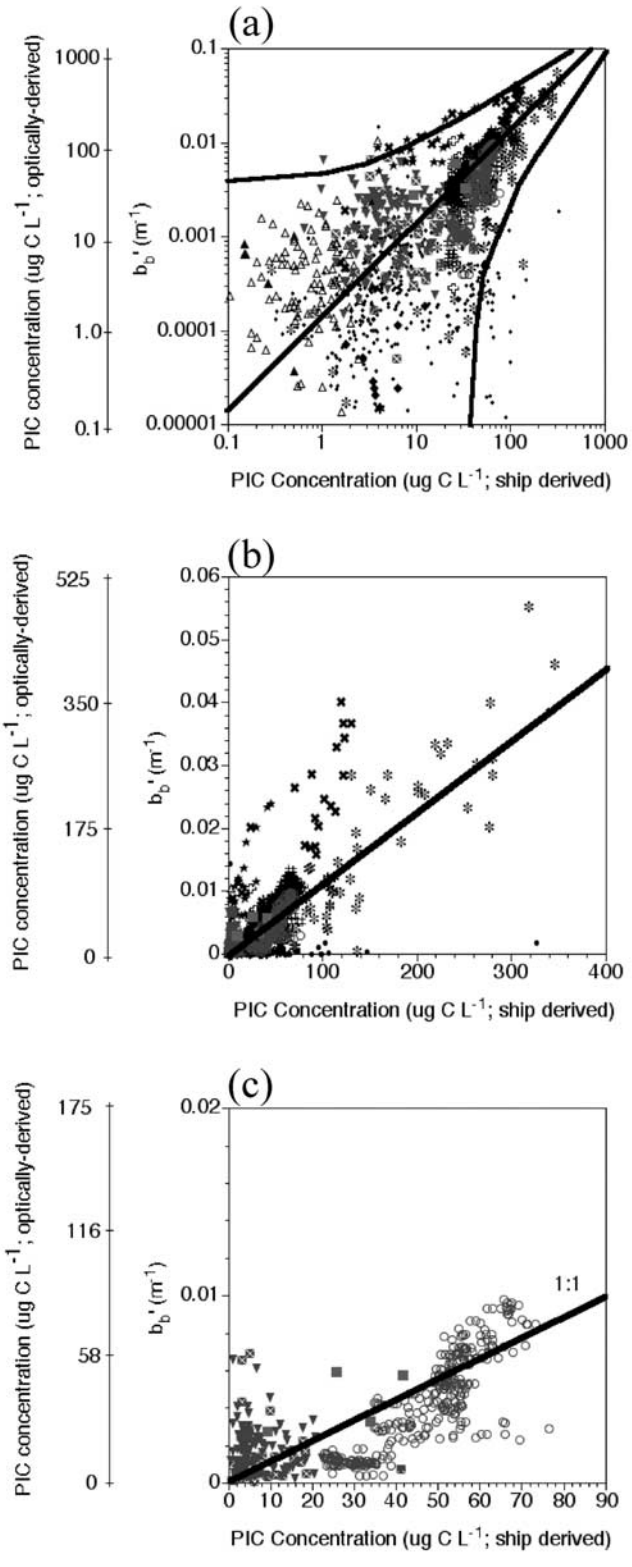

Figure 4. (a) Plot of optically derived PIC concentration versus ship-measured values (based on inductively coupled plasma atomic absorption spectrometry measurements of particulate material). The *y* axis includes an extra scale with the intermediate acid-labile backscattering value (b'_b) used to optically estimate PIC. Conversion of b'_b to PIC assumes 1.37 m^2 mol PIC^{-1} = 1.14 × 10^{-4} m^2 [mg PIC]$^{-1}$. The data sets used to make this plot were 1991 Iceland coccolithophore bloom (asterisks), Arabian Sea 1995 (open triangles), Straits of Florida 1995 (solid triangles), flow cytometer analysis of sorted coccoliths (solid stars), Gulf of Maine Ferry 1998–2001 (solid dots), Chalk-Ex ship measurements November 2001 (black crosses), Moderate-Resolution Imaging Spectroradiometer (MODIS) Gulf of Maine 2000–2001 (shaded squares with white cross within), Sea-viewing Wide Field-of-view Sensor (SeaWiFS) Gulf of Maine 1998–2001 (solid inverted triangles), Gulf of Maine coccolithophore bloom ship measurements (open crosses, pound symbols), Gulf of Maine July 2002 coccolithophore bloom MODIS measurements (open circles), and Chalk-Ex MODIS measurements November 2001 (solid shaded squares). There are both satellite and ship data shown in this plot. The two bold, black, curved lines that enclose the data distribution were drawn by eye. The bold straight line is the least squares linear fit to the data, with the standard error given in parentheses [b'_b(0.0033) = 1.145E-4 (1.576E-6) × PIC; r^2 = 0.60; n = 1783; RMS error in PIC concentration = 28.56 ug PIC L^{-1}; $P < 0.001$]. (b) Same as Figure 4a, but using linear axes instead of log axes. The complete statistics for the plot are the same as in Figure 4a. (c) Same as Figures 4a and 4b, except only satellite-derived PIC data are shown. The bold straight line is the 1:1 line for PIC. The equation describing the best least squares linear fit to the data is [b'_b = 9.665E-5 × PIC; r^2 = 0.55; n = 463; RMS error in PIC concentration = 14.9 ug PIC L^{-1}; $P <$ 0.001].

Table 2. Standard Error Estimates for Remote Particulate Inorganic Carbon (PIC) Measurements Binned at Different Timescales and Space Scales[a]

	Spatial Resolution, km			
Time Bins, days	1	4.63	36	111.2
1	14.90	3.218	**0.414**	**0.134**
8	5.632	**1.216**	**0.156**	**0.051**
30	2.720	**0.588**	**0.076**	**0.024**
365	**0.780**	**0.168**	**0.022**	**0.007**

[a]PIC measurements are in μg PIC L^{-1}. The 111.2 km spatial scale is equivalent to 1 degree of latitude. Bold values show binning, which provides a standard error less than globally averaged PIC of ~2 μg PIC L^{-1}.

Space/time binning clearly allowed more confidence in interpreting global images of surface PIC.

4. Discussion

4.1. Potential Interactions From Other Suspended Minerals

[26] A potential source of error, not considered in the PIC algorithm, was the presence of other suspended minerals in the water, such as large concentrations of diatom silica (opal). The data used to make the two-band PIC algorithm were from the field, and indeed contained diatoms and their associated opal silica. Thus some degree of "opal contamination" is already inherent in the algorithm, which likely contributed to its overall error budget (but also we implicitly compensated for the presence of this mineral since it occurs naturally in the same seawater that the original algorithm was derived from). Nonetheless, it is well known that there are regions of the ocean that can have high concentrations of diatoms (e.g., Southern Ocean [*Brzezinski et al.*, 2001]). In the Bering Sea, some regions of high scattering, once thought to be caused by coccolithophores, have been shown to be resuspended diatom frustrules from the sea floor [*Broerse et al.*, 2003]. Thus the issue is to define the error in the PIC algorithm when the opal:PIC ratio in surface waters was different from that used in the original algorithm development. In other words, we need to define how robust the PIC algorithm was under typical and atypical oceanic concentrations of biogenic silica.

[27] A first-order estimate of the error from suspended silica can be made quite easily. *Brzezinski et al.* [2001] observed concentrations of 12–16 μmol of biogenic silica per liter in intense diatom blooms in the Southern Ocean. In our laboratory, we have measured the mass-specific backscattering coefficient of suspended diatom frustules (0.624 m^2 $(mol\ Si)^{-1}$) [*Broerse et al.*, 2003]. Thus the amount of Si observed by Brzezinski would contribute 7.5×10^{-3} to 10×10^{-3} m^{-1} of backscattering over and above that due to POC- or PIC-containing particles. This quantity of biogenic silica in a diatom bloom indeed could cause significant error in the PIC determination. However, more typical biogenic silica concentrations (1–3 μmol L^{-1}) would only produce additional backscattering of 0.62×10^{-3} to 1.87×10^{-3} m^{-1}; such quantities likely are already "built into" the current PIC algorithm. In short, the extent of error due to biogenic silica cannot be estimated until radiometric data sets become available that would allow the partitioning of variance between opal and calcium carbonate.

4.2. Recent Observations of Global Particulate Inorganic Carbon (PIC)

[28] The launch of MODIS/Terra and MODIS/Aqua, along with the above-described validation results, have allowed the first opportunities to map global PIC with definable errors (Table 2). We have assembled version 4.1 MODIS/Terra data from 2002 into images of seasonal

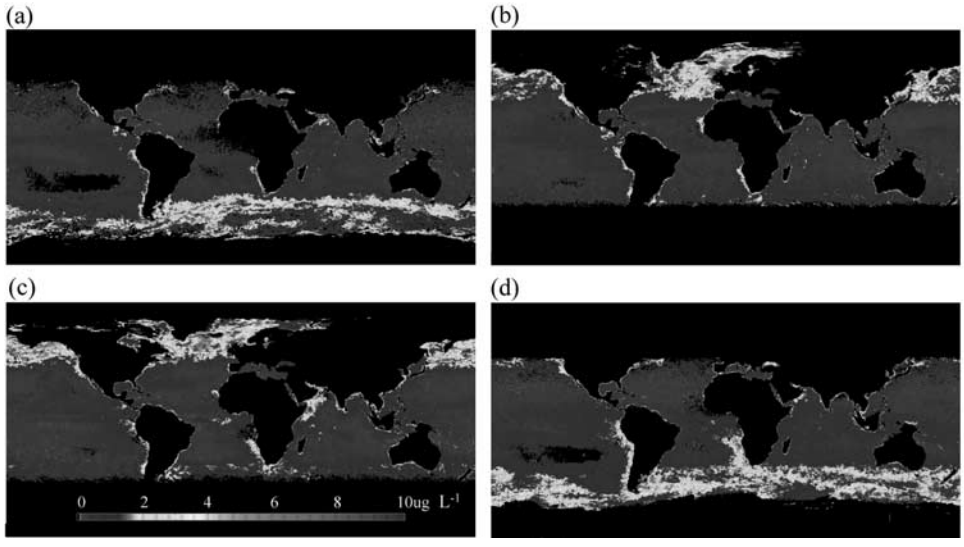

Figure 5. Global composite images of suspended PIC concentration calculated from MODIS/Terra data using two-band calcite algorithm. See text for other details of how the data were processed. The color scale is highlighted in Figure 5c. These data were binned into 36 km and 90 day averages, and thus the standard error will be <0.08 μgPIC L^{-1} (see Table 2), well below the average seawater concentration of ~2 μgPIC L^{-1}. (a) January–March. (b) April–June. (c) July–September. (d) October–December. See color version of this figure at back of this issue.

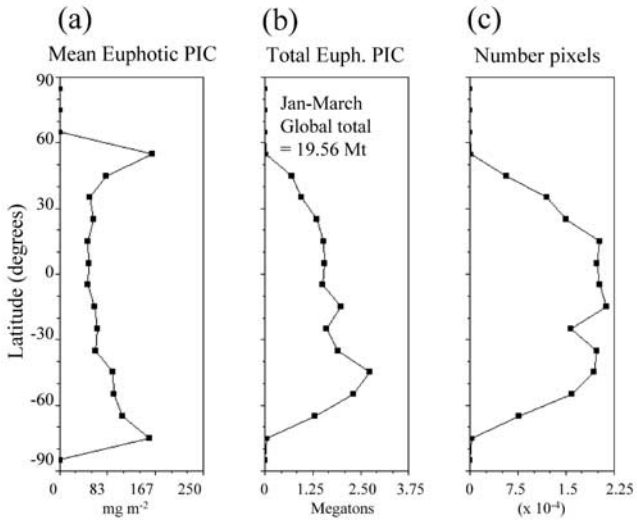

Figure 6. Statistics for 2002 PIC estimates as a function of latitude between January and March. (a) Mean PIC integrated over the euphotic zone. (b) Total euphotic zone PIC, integrated aerially in each latitudinal band. (c) Number of pixels analyzed in each latitudinal band. See text for details.

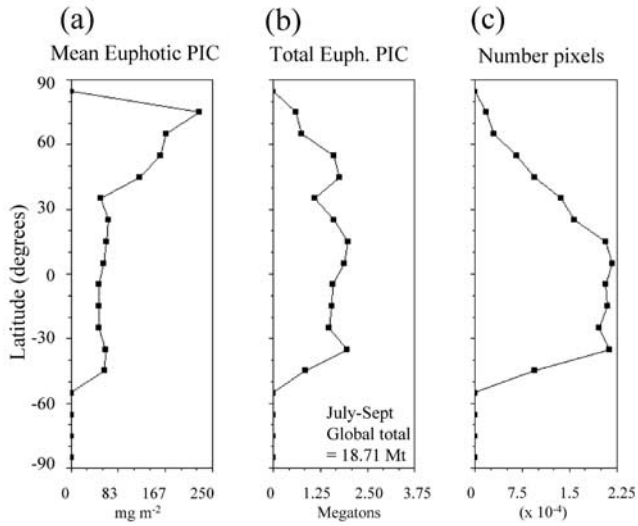

Figure 8. Statistics for PIC estimates as a function of latitude between July and September 2002. All else is identical to Figure 6.

average PIC (Figure 5). There were some striking features in these data. From October to March (including Austral spring and summer), there were large regions of the Polar Convergence Zone and subpolar front that appear to have relatively high concentrations of PIC. Note, the peak concentration shown in Figure 5 is 10 μg PIC L^{-1}, which, by no means should be considered a discolored coccolithophore bloom, but still is significantly higher than typical values seen in the central ocean gyres. From April to September (including Northern Hemisphere spring and summer) the Bering Sea, North Atlantic and Barents Sea showed high concentrations of PIC. The Namibian upwelling region, off of West Africa, showed dramatic increases in PIC concentration between October and December (Figure 5d).

[29] Given the seasonal images in Figure 5, we integrated the total surface PIC over the euphotic zone, within 10° latitudinal bands (Figures 6–9; Tables 3 and 4). First, the depth of the euphotic zone was estimated using satellite-derived chlorophyll concentration; the MODIS product "chlor-a2" was used as input to the algorithm for calculation of the average K_{par} over the euphotic zone to the 1% light depth [*Morel*, 1988, equation (5)]. We then made the first-order assumption, admittedly over simplified but still reasonable based on field PIC results in non-bloom conditions, that the concentration of PIC was vertically uniform over the euphotic zone.

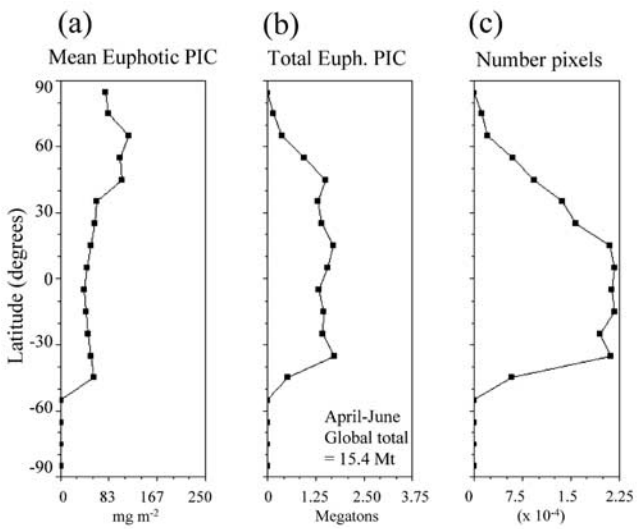

Figure 7. Statistics for PIC estimates as a function of latitude between April and June 2002. All else is identical to Figure 6.

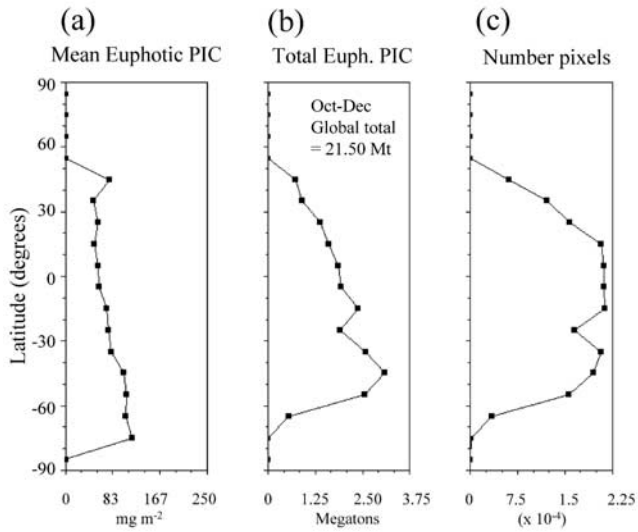

Figure 9. Statistics for PIC estimates as a function of latitude between October and December 2002. All else is identical to Figure 6.

Table 3. Total Euphotic Zone PIC as a Function of Season in 2002, Estimated From the Surface to the 1% Light Level[a]

	Midpoint of 10° Latitudinal																		All
	85	75	65	55	45	35	25	15	5	−5	−15	−25	−35	−45	−55	−65	−75	−85	Latitudes
Jan–Feb	0.00	0.00	0.00	0.03	0.71	0.95	1.35	1.54	1.56	1.51	1.98	1.60	1.92	2.74	2.32	1.30	0.04	0.00	19.56
Mar–Jun	0.00	0.14	0.37	0.95	1.51	1.31	1.42	1.70	1.55	1.33	1.45	1.43	1.72	0.52	0.00	0.00	0.00	0.00	15.40
Jul–Sep	0.00	0.61	0.75	1.60	1.75	1.11	1.60	1.97	1.89	1.58	1.56	1.47	1.97	0.85	0.00	0.00	0.00	0.00	18.71
Oct–Dec	0.00	0.00	0.00	0.00	0.72	0.91	1.38	1.61	1.85	1.93	2.40	1.92	2.59	3.08	2.56	0.55	0.01	0.00	21.50

[a]Values given in 10° latitude increments (in megatons of carbon). These same data are graphed in Figures 6b, 7b, 8b, and 9b. Values of 0.00 represent regions with no satellite radiance estimates available, mostly due to low Sun angle at high latitudes.

[30] Equation (25) of *Morel* [1988] (POC = 90 $C^{0.57}$) provided a means to estimate surface POC (mg m^{-3}) based on the mean remotely sensed pigment concentration, *C*. The pigment data used to generate *Morel*'s [1988] relationship were sampled from a variety of environments ranging from oligotrophic to eutrophic regions (n = 409), spanning over three orders of magnitude of pigment concentration. Moreover, this relationship reasonably provided a range in the carbon:chlorophyll ratio of 1000 in the most oligotrophic environments to 25 in eutrophic environments, which is the typical range of field observations [*Eppley et al.*, 1977; *Geider*, 1987; *Steele and Baird*, 1962]. In order to integrate the POC values to the base of the euphotic zone, we assumed a constant POC concentration with depth. We caution that this only provides a first-order estimate of euphotic POC since there is well known vertical heterogeneity in phytoplankton biomass over the euphotic zone [*Cullen*, 1990].

[31] Seasonal global totals of euphotic PIC (within all latitudes visible to the satellite) ranged from 15.4–21.5 Mt PIC (Figures 6–9). Moreover, the results demonstrated two global patterns of PIC distribution over the year. The first pattern prevailed between October and March, when about 69% of the PIC was in the Southern Hemisphere. During the period between April and September, the pattern shifted hemispheres, but not symmetrically; about 59% of the PIC was in the Northern Hemisphere during this period. It is clear from the images (Figure 5) that the bands with elevated PIC in the Southern Hemisphere represented a large fraction of the total global euphotic PIC. About 40% of the global PIC was found south of 30°S between October and March compared to the April to September period in the Northern Hemisphere (in which ~29% of the PIC was found north of 30°N). Unfortunately, as of this writing, few shipboard data exist that could be used to validate these regions of elevated PIC in the Southern Convergence Zone.

4.3. Regional Analysis of PIC Distributions

[32] To provide more quantitative regional estimates of the global PIC standing stock, we used the biogeographic provinces described by *Longhurst* [1998] and calculated the average surface PIC concentration and its variance within each province over a season (Table 5). Owing to the high PIC concentrations observed in the Black Sea and Persian Gulf, we added separate provinces to *Longhurst*'s [1998] original list. The Caspian Sea is not included in our budget calculations due to its isolation from the global ocean. The Chesapeake Bay province listed by *Longhurst* [1998] also is not included here due to its small size. To aid in global estimates, we also generated a table of average integrated euphotic zone PIC concentration (calculated as described above) and its standard deviation within each biogeochemical province (Table 6).

[33] Tabular budgets of surface PIC concentration demonstrate some striking trends. The seasonal average PIC concentration (Table 5) for all provinces was 2 μg PIC L^{-1} (which varied from 1.9–2.2 μg PIC L^{-1}). Clearly, the PIC concentrations within the Trades biome were consistently the lowest, regardless of season, averaging 0.66–0.81 μg PIC L^{-1}. Northern polar biomes (including boreal polar, Atlantic Arctic, Atlantic Subarctic, North Pacific Epicontinental) consistently showed above average PIC concentrations, at least when they were visible to the MODIS sensor between April and September. Northern polar PIC concentrations were highest between July and September 2002. The Atlantic Subarctic province, within the polar biome, showed 2–3 × the global average PIC concentration during those months, fully consistent with previous observations of mesoscale coccolithophore blooms in these areas [*Balch et al.*, 1992, 1996a, 1996b; *Brown and Yoder*, 1994; *Fernández et al.*, 1993; *Holligan et al.*, 1993]. Southern polar biomes, when visible to MODIS/Terra between October and March, showed PIC concentrations slightly lower than the Northern Hemisphere polar biome. There are few validation measurements from this region to confirm these MODIS estimates. Coastal provinces had the greatest PIC concentrations of all the biomes, averaging between 2.5 to 3.8 μg PIC L^{-1}, depending on the season. As might be expected, the variance in PIC concentration was greatest over space and time in the coastal provinces.

[34] Specific provinces that had above average PIC concentrations, in at least one 3 month period, were: boreal polar, Atlantic arctic, Atlantic subarctic, North Pacific epicontinental, Black Sea, Pacific subarctic gyres (east and west), northeast Atlantic Shelves, Canary coastal, Guianas coastal, northwest Atlantic shelves, southwest Atlantic shelves, Benguela Current Coastal, Persian Gulf, east India Coastal, west India Coastal, Australia west, Alaska downwelling coastal, China Sea Coastal and New Zealand Coastal. The observations of coastal shelf coccolithophore blooms are consistent with historical remote sensing observations from a number of these areas such

Table 4. Percentage of Total Global, Euphotic PIC Poleward of 30° Latitude or the Equator as a Function of Season in 2002

	Jan–Mar	Apr–Jun	Jul–Sep	Oct–Dec
% PIC N of 30°N	8.65	27.80	31.07	7.57
% PIC S of 30°S	42.55	14.59	15.08	40.88
% PIC N Hemisphere	31.39	58.07	60.30	30.10
% PIC S Hemisphere	68.61	41.93	39.70	69.90

Table 5. Surface PIC Aerially Integrated Within the Biogeochemical Provinces Defined by *Longhurst* [1998][a]

Surface PIC		Jan–Mar Average					Apr–Jun Average					Jul–Sep Average					Oct–Dec Average				
Province	Biome	Tot. PIC, Mt	Surf. PIC, mg/m^3	SD, mg/m^3	PIC:POC	Pixels	Tot. PIC, Mt	Surf. PIC, mg/m^3	SD, mg/m^3	PIC:POC	Pixels	Tot. PIC, Mt	Surf. PIC, mg/m^3	SD, mg/m^3	PIC:POC	Pixels	Tot. PIC, Mt	Surf. PIC, mg/m^3	SD, mg/m^3	PIC:POC	Pixels
Boreal Polar	polar	0.0000	0.00	0.00	NA	0	0.0031	2.27	1.34	0.029	2606	0.0167	4.12	2.05	0.064	7123	0.0000	0.00	0.00	NA	0
Atl Arctic	polar	0.0000	0.00	0.00	0.000	0	0.0067	2.20	0.47	0.031	4803	0.0111	3.54	1.12	0.058	4982	0.0000	0.00	0.00	NA	0
Atl Subarctic	polar	0.0000	0.00	0.00	NA	0	0.0082	4.11	0.99	0.047	3225	0.0125	6.32	2.40	0.093	3208	0.0000	0.00	0.00	NA	0
N Pac Epicontinental	polar	0.0008	1.56	0.99	0.029	491	0.0121	3.40	1.35	0.037	3952	0.0130	3.29	1.15	0.050	4420	0.0010	1.83	1.14	0.032	501
Antarctic	polar	0.0354	1.85	0.78	0.048	25137	0.0000	0.00	0.00	NA	0	0.0000	0.00	0.00	NA	0	0.0257	1.77	0.47	0.045	18530
Austral Polar	polar	0.0096	2.56	0.86	0.045	6139	0.0000	0.00	0.00	NA	0	0.0000	0.00	0.00	NA	0	0.0007	1.61	0.94	0.039	685
N Atl Drift(WWDR)	westerlies	0.0017	1.73	3.42	0.050	923	0.0097	2.73	1.03	0.041	3606	0.0083	2.34	1.10	0.043	3608	0.0004	0.65	0.21	0.017	508
Gulf Stream	westerlies	0.0011	1.71	2.60	0.035	554	0.0012	1.07	0.33	0.020	996	0.0010	0.84	0.60	0.027	996	0.0008	1.02	1.32	0.026	686
N Atl Subtrop Gyre (W)	westerlies	0.0025	0.49	0.29	0.017	3902	0.0041	0.68	0.32	0.026	4622	0.0035	0.58	0.13	0.030	4622	0.0023	0.41	0.18	0.017	4415
Mediterranean Sea	westerlies	0.0028	1.10	1.01	0.026	2074	0.0024	0.93	0.71	0.028	2115	0.0016	0.61	0.42	0.023	2106	0.0029	1.22	1.44	0.036	1978
Black Sea	westerlies	0.0024	6.07	1.43	0.070	349	0.0098	25.04	4.69	0.299	348	0.0051	12.96	2.75	0.181	350	0.0023	6.17	2.04	0.086	329
N Atl Subtrop Gyre (E)	westerlies	0.0023	0.62	0.50	0.018	2891	0.0071	1.60	1.17	0.036	3559	0.0024	0.55	0.19	0.021	3558	0.0018	0.47	0.33	0.016	3034
Pac Subarctic Gyres (E)	westerlies	0.0004	0.65	0.26	0.017	584	0.0052	1.63	0.74	0.029	3307	0.0132	4.18	1.05	0.079	3292	0.0008	1.51	0.40	0.033	473
Pac Subarctic Gyres (W)	westerlies	0.0008	0.81	0.42	0.020	906	0.0041	1.88	0.79	0.029	2097	0.0089	4.02	1.28	0.067	2133	0.0014	1.32	0.40	0.028	982
Kuroshio Current	westerlies	0.0030	1.11	2.31	0.026	2084	0.0049	1.53	0.94	0.029	2512	0.0034	1.05	0.72	0.030	2497	0.0028	1.02	1.95	0.027	2116
N Pac Polar Front	westerlies	0.0041	0.67	0.24	0.017	5125	0.0092	1.30	0.57	0.030	5996	0.0075	1.03	0.58	0.033	6157	0.0052	0.78	0.30	0.021	5646
N Pac Subtrop Gyre	westerlies	0.0054	0.40	0.20	0.019	9567	0.0066	0.48	0.20	0.023	9837	0.0064	0.46	0.10	0.026	9839	0.0053	0.40	0.18	0.020	9584
Tasman Sea	westerlies	0.0011	0.65	0.28	0.021	1384	0.0018	1.07	1.20	0.023	1372	0.0023	1.36	1.74	0.030	1370	0.0028	1.65	0.77	0.034	1386
S Pac Subtrop Gyre	westerlies	0.0158	0.57	0.27	0.032	19687	0.0180	0.51	0.23	0.021	25391	0.0194	0.55	0.27	0.021	25571	0.0237	0.80	0.36	0.037	21359
S Subtrop Convergence	westerlies	0.0225	1.31	0.67	0.036	14724	0.0129	0.94	0.45	0.022	11578	0.0143	0.93	0.67	0.025	13039	0.0282	1.64	0.62	0.040	14790
Subantarctic	westerlies	0.0513	1.65	0.69	0.042	31157	0.0033	1.18	0.65	0.027	2450	0.0046	0.80	0.49	0.023	5189	0.0600	1.90	0.59	0.045	31728
N Atl Trop Gyre	trades	0.0050	0.68	3.60	0.029	5024	0.0064	0.81	3.11	0.030	5489	0.0061	0.76	3.05	0.032	5514	0.0051	0.66	3.40	0.027	5360
W Trop Atl	trades	0.0021	0.53	0.56	0.019	2564	0.0032	0.59	0.28	0.017	3514	0.0036	0.66	0.35	0.019	3535	0.0032	0.62	0.30	0.020	3314
East Trop Atl	trades	0.0013	0.49	0.19	0.015	1758	0.0028	0.55	0.22	0.014	3351	0.0043	0.94	0.42	0.022	2981	0.0045	0.97	0.31	0.028	3048
S Atl Gyre	trades	0.0112	0.64	0.32	0.032	12750	0.0104	0.58	0.21	0.020	13133	0.0133	0.75	0.38	0.024	12893	0.0197	1.12	0.66	0.040	12847
Caribbean	trades	0.0079	1.90	4.65	0.054	2872	0.0051	1.23	3.50	0.038	2875	0.0057	1.38	3.45	0.043	2875	0.0073	1.77	4.53	0.051	2871
Indian Monsoon Gyres	trades	0.0084	0.54	0.34	0.020	10282	0.0074	0.47	0.31	0.016	10287	0.0113	0.72	0.51	0.021	10284	0.0107	0.69	0.32	0.023	10270
Indian S Subtrop Gyre	trades	0.0092	0.53	0.17	0.030	12392	0.0095	0.55	0.22	0.020	12405	0.0105	0.61	0.27	0.020	12407	0.0121	0.70	0.25	0.031	12400
N Pac Trop Gyre	trades	0.0060	0.44	0.26	0.020	9584	0.0076	0.51	0.16	0.024	10511	0.0080	0.54	0.15	0.026	10586	0.0058	0.40	0.20	0.019	10281
N Pac Eq Countercurrent	trades	0.0057	0.64	0.31	0.019	5918	0.0073	0.81	0.69	0.023	5946	0.0065	0.73	0.30	0.025	5929	0.0060	0.67	0.24	0.024	5941
Pac Eq Divergence	trades	0.0087	0.60	0.28	0.019	9489	0.0083	0.57	0.23	0.016	9492	0.0092	0.64	0.34	0.019	9385	0.0108	0.75	0.39	0.024	9444
W Pac Warm Pool	trades	0.0059	0.48	0.23	0.024	8099	0.0057	0.46	0.14	0.021	8191	0.0065	0.52	0.16	0.024	8190	0.0064	0.52	0.18	0.025	8190
Archipelagic Deep Basins	trades	0.0076	0.82	2.13	0.030	6294	0.0068	0.74	1.52	0.024	6321	0.0088	0.96	1.72	0.027	6317	0.0076	0.82	1.47	0.029	6340
NE Atl Shelves	coastal	0.0018	19.00	9.12	0.258	95	0.0042	6.52	2.74	0.050	777	0.0027	4.40	1.57	0.050	738	0.0001	6.28	5.19	0.130	13
Canary Coastal (EACB)	coastal	0.0018	2.76	2.90	0.036	480	0.0022	3.26	2.71	0.034	498	0.0011	1.75	1.59	0.032	485	0.0015	2.38	2.42	0.045	465
Guinea Current Coastal	coastal	0.0005	1.35	1.08	0.024	242	0.0012	1.21	1.72	0.020	642	0.0011	1.65	1.09	0.032	429	0.0013	1.73	1.22	0.034	484
Guianas Coastal	coastal	0.0054	4.49	7.87	0.075	796	0.0042	3.41	6.18	0.046	812	0.0046	3.82	7.45	0.061	798	0.0060	4.88	9.10	0.085	811
NW Atl Shelves	coastal	0.0058	4.33	5.49	0.067	1152	0.0054	2.60	2.98	0.031	1877	0.0086	4.10	3.89	0.071	1898	0.0041	3.06	3.91	0.054	1150
Brazil Current Coastal	coastal	0.0012	1.19	1.50	0.031	724	0.0015	1.51	1.90	0.036	723	0.0018	1.79	2.62	0.041	720	0.0016	1.55	2.09	0.037	728
SW Atl Shelves	coastal	0.0048	3.69	1.58	0.040	1311	0.0003	2.30	1.30	0.031	112	0.0021	6.94	6.96	0.111	278	0.0067	5.17	2.36	0.059	1310
Benguela Current Coastal	coastal	0.0031	2.85	2.52	0.040	783	0.0022	2.04	1.25	0.026	775	0.0027	2.61	1.23	0.040	752	0.0044	4.13	2.11	0.057	779
E Africa Coastal	coastal	0.0045	1.28	1.81	0.037	2565	0.0051	1.45	2.37	0.032	2566	0.0064	1.82	3.17	0.041	2567	0.0056	1.59	2.30	0.042	2568
Red Sea	coastal	0.0008	1.82	2.34	0.036	318	0.0007	1.46	1.68	0.035	330	0.0006	1.37	1.71	0.035	328	0.0008	1.72	1.85	0.036	321
Persian Gulf	coastal	0.0017	9.88	7.57	0.099	124	0.0007	4.28	2.36	0.050	125	0.0006	3.64	2.37	0.056	126	0.0016	9.29	7.97	0.122	125
NW Arabian Upwelling	coastal	0.0042	1.23	1.30	0.019	2322	0.0032	0.95	1.24	0.021	2267	0.0071	2.35	1.84	0.036	2032	0.0046	1.33	0.93	0.025	2325
E India Coastal	coastal	0.0022	2.43	4.75	0.041	611	0.0026	2.89	5.40	0.050	620	0.0037	4.32	6.47	0.079	589	0.0025	3.45	5.64	0.060	502
W India Coastal	coastal	0.0035	4.33	7.96	0.055	542	0.0030	3.75	7.85	0.052	540	0.0035	5.32	8.57	0.064	443	0.0028	3.50	6.51	0.050	546
Australia West	coastal	0.0038	1.38	2.16	0.041	1961	0.0060	2.19	3.09	0.047	1965	0.0082	2.95	4.47	0.064	1976	0.0045	1.63	2.14	0.044	1966

Table 5. (continued)

Surface PIC		Jan–Mar Average					Apr–Jun Average					Jul–Sep Average					Oct–Dec Average				
Province	Biome	Tot. PIC, Mt	Surf. PIC, mg/m^3	SD, mg/m^3	PIC:POC	Pixels	Tot. PIC, Mt	Surf. PIC, mg/m^3	SD, mg/m^3	PIC:POC	Pixels	Tot. PIC, Mt	Surf. PIC, mg/m^3	SD, mg/m^3	PIC:POC	Pixels	Tot. PIC, Mt	Surf. PIC, mg/m^3	SD, mg/m^3	PIC:POC	Pixels
Alaska Downwelling Coastal	coastal	0.0000	0.92	0.00	0.017	2	0.0018	3.74	1.57	0.032	562	0.0022	4.57	1.93	0.058	554	0.0000	0.00	0.00	NA	0
California Upwelling Coastal	coastal	0.0028	1.25	1.68	0.027	1747	0.0047	1.84	1.34	0.032	2042	0.0045	1.67	1.41	0.037	2166	0.0030	1.30	1.34	0.031	1818
Centr American Coastal	coastal	0.0025	2.14	3.02	0.032	791	0.0024	2.09	2.10	0.032	787	0.0025	2.17	3.88	0.047	777	0.0025	2.13	2.92	0.042	785
Chile	coastal	0.0049	2.00	1.57	0.033	1873	0.0042	2.02	1.51	0.029	1517	0.0038	1.98	1.35	0.035	1438	0.0065	2.71	1.39	0.045	1867
China Sea Coastal	coastal	0.0080	12.57	13.56	0.159	471	0.0020	2.85	3.39	0.045	514	0.0019	2.70	3.72	0.054	520	0.0053	7.81	9.20	0.130	498
Sunda	coastal	0.0093	2.47	4.65	0.059	2490	0.0064	1.66	3.41	0.040	2528	0.0074	1.94	3.56	0.047	2524	0.0086	2.24	4.45	0.058	2532
East Australian Coastal	coastal	0.0008	0.77	0.97	0.031	748	0.0008	0.80	0.99	0.023	746	0.0010	0.99	1.15	0.027	750	0.0009	0.87	0.87	0.030	751
New Zealand Coastal	coastal	0.0021	1.73	1.05	0.037	1108	0.0011	2.80	3.63	0.051	341	0.0012	1.89	2.20	0.042	579	0.0031	2.60	1.39	0.050	1110
Unclassified	coastal	0.0004	1.03	2.47	0.034	347	0.0005	1.27	5.31	0.034	307	0.0007	1.71	5.93	0.049	327	0.0005	1.11	1.93	0.038	324
Summary		**0.3175**	**2.12**	**3.16**	**0.048**	**238307**	**0.2771**	**2.13**	**3.33**	**0.041**	**209860**	**0.3290**	**2.23**	**2.17**	**0.051**	**218750**	**0.3460**	**1.90**	**1.92**	**0.048**	**232814**
Polar		**0.046**	**1.99**	**0.88**	**0.040**	**31767**	**0.030**	**2.99**	**1.04**	**0.036**	**14586**	**0.053**	**4.32**	**1.68**	**0.067**	**19733**	**0.027**	**1.73**	**0.85**	**0.038**	**19716**
Westerlies		**0.117**	**1.30**	**0.97**	**0.033**	**95911**	**0.100**	**2.84**	**0.94**	**0.060**	**79786**	**0.102**	**2.15**	**0.81**	**0.057**	**84327**	**0.141**	**1.40**	**0.74**	**0.036**	**99014**
Trades		**0.079**	**0.69**	**1.09**	**0.026**	**87026**	**0.080**	**0.66**	**0.88**	**0.022**	**91515**	**0.094**	**0.77**	**0.93**	**0.025**	**90896**	**0.099**	**0.81**	**1.02**	**0.029**	**90306**
Coastal		**0.075**	**3.73**	**3.76**	**0.062**	**23256**	**0.066**	**2.51**	**2.73**	**0.037**	**23666**	**0.079**	**2.90**	**3.23**	**0.052**	**23467**	**0.078**	**3.10**	**3.36**	**0.060**	**23454**

[a]Provinces are grouped into their respective biome: Polar, Westerlies, Trades, and Coastal. Calculations have been made for each 3 month period of 2002. Results are given for each province for (1) total PIC (essentially, the total PIC found in the top meter of the water column, aerially integrated over the province), (2) average surface PIC (mg m^{-3}), (3) standard deviation of the average PIC (mg m^{-3}), (4) PIC:POC ratio (where PIC was taken from the average value in the second column of each 3 month period and POC was taken from the same column of Table 7), and (5) the total number of pixels available for the analysis. Any values of 0.00 in the first three columns of the polar biome for each 3 month period represent regions where no satellite radiance data were available, mainly due to low Sun angle. At the bottom of the table the global statistics are provided as well as statistics for each of the four biomes.

as the northwest Atlantic shelves [*Ackleson et al.*, 1994; *Balch*, 2004; *Balch et al.*, 1991; *Keller et al.*, 1992; *Matrai and Keller*, 1993; *Townsend et al.*, 1994], the northeast Atlantic shelves [*Berge*, 1962; *Birkenes and Braarud*, 1952; *Brown and Yoder*, 1994; *Brussaard et al.*, 1996; *Buitenhuis et al.*, 1996; *Burkill et al.*, 2002; *Garcia-Soto et al.*, 1995; *GREPMA*, 1981; *Head et al.*, 1998; *Holligan et al.*, 1983; *Malin et al.*, 1993; *Samtleben and Bickert*, 1990; *Van der Wal et al.*, 1995; *Wal et al.*, 1995], Australian coastal [*Blackburn and Cresswell*, 1993], Alaska downwelling and North Pacific Epicontinental [*Kai et al.*, 1999; *Lavrentyev et al.*, 2001; *Napp and Hunt*, 2001; *Stockwell et al.*, 2000; *Takahashi et al.*, 1995; *Broerse et al.*, 2003], Black Sea [*Cokacar*, 2001], the southwest Atlantic shelves [*Gayoso*, 1995], and Pacific subarctic gyres [*Fukushima and Ishizaka*, 1993; *Takahashi et al.*, 1995].

[35] Satellite-derived PIC concentrations can be checked for consistency using independent ship measurements from the same area. Note, however, this approach only allows for a gross comparison of the PIC levels since the ship and satellite observations, while measured in the same season, were made in different years. Satellite-derived values of 0.64 ± 0.34 μg PIC L^{-1} were observed in the Pacific equatorial divergence province during July–September 2002 (Table 5). These were lower than the average shipboard value of 2.52 (±0.58) μg PIC L^{-1} described by *Balch and Kilpatrick* [1996] for the period between August and September 1992, between 5°N and 5°S along 140°W, top 10 m only (n = 17; note one anomalously high surface value of 15 μg PIC L^{-1} at 2°N was not included in this average). Satellite-derived PIC values from the NW Arabian upwelling province were estimated to be 2.35 ± 1.84 μg PIC L^{-1} during August–September 2002 (Table 5). During July and August 1995, the average PIC measured by *Balch et al.* [2000] in the Arabian Sea was 2.38 ± 2.14 μg PIC L^{-1} [see *Balch et al.*, 2000, Table 1], not significantly different from the satellite-derived value. During October and November 1995, average PIC concentrations measured by *Balch et al.* [2000] were 1.62 ± 2.03 μg PIC L^{-1}, also not significantly different from the satellite-derived values between October and December 2002 (1.33 ± 0.93 μg PIC L^{-1} (Table 5)).

[36] A different view of the PIC budget can be seen in the table of PIC concentrations integrated over the euphotic zone, and aerially over each province (Table 6). The average integrated concentrations of PIC approximately mirrored the trends in surface concentration described above (but not exclusively). Aerially integrating over the various biomes, the majority of the euphotic standing stock of calcium carbonate (70–77%) occurred in the combined Westerlies and Trades biomes. This is consistent with results suggesting that low-latitude, nonbloom coccolithophores are responsible for large export ratios of $CaCO_3$: organic matter [*Sarmiento et al.*, 2002]. While the polar biomes had the highest concentrations of PIC, they only contributed 7–12% of the total PIC and the coastal biomes contributed ~15%. Note, however, these polar values are likely underestimates during the fall and winter months of each hemisphere, since no satellite-derived radiance estimates are possible due to low Sun angle. Provinces that contributed over 0.5 Mt of PIC (greater than ~2% of the global total PIC) for at least one 3 month

Table 6. Euphotic Zone PIC Aerially Integrated Within the Biogeochemical Provinces Defined by *Longhurst* [1998][a]

Int. PIC Over Euphotic Zone		Jan–Mar					Apr–Jun					Jul–Sep					Oct–Dec				
Province	Biome	Tot. PIC, Mt	% Total	Avg Int. PIC, mg/m^2	SD, mg/m^2	Pixels	Tot. PIC, Mt	% Total	Avg Int. PIC, mg/m^2	SD, mg/m^2	Pixels	Tot. PIC, Mt	% Total	Avg Int. PIC, mg/m^2	SD, mg/m^2	Pixels	Tot. PIC, Mt	% Total	Avg Int. PIC, mg/m^2	SD, mg/m^2	Pixels
Boreal Polar	polar	0.000	0.00	0.00	0.00	0	0.115	0.75	82.66	37.03	2606	0.662	3.54	162.77	70.05	7123	0.000	0.00	0.00	0.00	0
Atl Arctic	polar	0.000	0.00	0.00	0.00	0	0.265	1.72	87.36	17.63	4803	0.472	2.52	150.12	41.35	4982	0.000	0.00	0.00	0.00	0
Atl Subarctic	polar	0.000	0.00	0.00	0.00	0	0.277	1.80	138.89	32.08	3225	0.489	2.62	246.46	86.67	3208	0.000	0.00	0.00	0.00	0
N Pac Epicontinental	polar	0.037	0.19	67.95	39.08	491	0.379	2.46	105.89	33.84	3952	0.515	2.75	130.44	35.83	4420	0.043	0.20	77.61	41.00	501
Antarctic	polar	1.988	10.17	104.02	30.24	25137	0.000	0.00	0.00	0.00	0	0.000	0.00	0.00	0.00	0	1.493	6.95	102.92	22.16	18530
Austral Polar	polar	0.384	1.96	102.07	26.24	6139	0.000	0.00	0.00	0.00	0	0.000	0.00	0.00	0.00	0	0.041	0.19	91.22	43.59	685
N Atl Drift(WWDR)	westerlies	0.085	0.43	87.03	122.79	923	0.393	2.55	110.51	32.02	3606	0.369	1.97	103.83	37.27	3608	0.022	0.10	39.41	11.62	508
Gulf Stream	westerlies	0.048	0.24	73.74	90.51	554	0.059	0.38	50.47	10.50	996	0.067	0.36	57.60	27.54	996	0.043	0.20	53.74	52.55	686
N Atl Subtrop Gyre (W)	westerlies	0.192	0.98	37.82	18.95	3902	0.328	2.14	54.95	13.77	4622	0.360	1.92	60.22	16.49	4622	0.204	0.95	35.72	13.59	4415
Mediterranean Sea	westerlies	0.152	0.78	59.84	43.51	2074	0.154	1.00	59.56	32.46	2115	0.120	0.64	46.76	22.69	2106	0.174	0.81	71.82	67.83	1978
Black Sea	westerlies	0.082	0.42	210.41	47.44	349	0.347	2.26	889.93	150.72	348	0.197	1.05	501.79	86.32	350	0.087	0.40	235.63	62.42	329
N Atl Subtrop Gyre (E)	westerlies	0.146	0.75	40.24	22.37	2891	0.344	2.24	77.51	38.33	3559	0.199	1.07	44.94	11.35	3558	0.133	0.62	34.81	15.86	3034
Pac Subarctic Gyres (E)	westerlies	0.023	0.12	38.24	14.57	584	0.238	1.55	74.84	33.38	3307	0.636	3.40	200.60	45.77	3292	0.040	0.19	79.93	19.47	473
Pac Subarctic Gyres (W)	westerlies	0.044	0.22	45.62	21.63	906	0.162	1.06	75.22	27.06	2097	0.380	2.03	172.67	41.67	2133	0.072	0.33	67.60	17.75	982
Kuroshio Current	westerlies	0.150	0.77	55.57	67.75	2084	0.216	1.41	67.17	24.22	2512	0.206	1.10	64.40	26.64	2497	0.156	0.72	56.73	68.92	2116
N Pac Polar Front	westerlies	0.237	1.21	39.09	13.79	5125	0.498	3.24	70.45	24.79	5996	0.491	2.63	67.74	26.83	6157	0.319	1.49	48.05	16.05	5646
N Pac Subtrop Gyre	westerlies	0.530	2.71	39.44	17.72	9567	0.635	4.13	45.98	13.40	9837	0.688	3.68	49.83	12.14	9839	0.543	2.52	40.30	15.61	9584
Tasman Sea	westerlies	0.075	0.38	44.63	12.48	1384	0.090	0.58	53.73	45.20	1372	0.114	0.61	68.34	67.08	1370	0.140	0.65	83.21	30.63	1386
S Pac Subtrop Gyre	westerlies	1.633	8.36	59.32	29.48	19687	1.591	10.35	45.04	14.53	25391	1.609	8.60	45.27	16.50	25571	2.148	9.99	72.19	30.06	21359
S Subtrop Convergence	westerlies	1.347	6.89	78.49	27.00	14724	0.703	4.58	51.32	21.59	11578	0.858	4.59	55.93	28.88	13039	1.598	7.43	92.68	26.40	14790
Subantarctic	westerlies	2.959	15.14	95.27	29.49	31157	0.155	1.01	55.72	31.83	2450	0.285	1.53	49.61	21.62	5189	3.334	15.50	105.57	24.78	31728
N Atl Trop Gyre	trades	0.344	1.76	47.38	135.15	5024	0.445	2.89	56.02	99.73	5489	0.445	2.38	55.77	101.43	5514	0.339	1.58	43.81	113.76	5360
W Trop Atl	trades	0.157	0.80	40.17	22.39	2564	0.206	1.34	38.46	11.53	3514	0.230	1.23	42.71	16.12	3535	0.226	1.05	44.78	17.27	3314
East Trop Atl	trades	0.099	0.51	37.00	15.34	1758	0.172	1.12	33.65	10.63	3351	0.235	1.26	51.77	18.23	2981	0.294	1.37	63.27	17.91	3048
S Atl Gyre	trades	1.115	5.71	63.91	26.65	12750	0.798	5.19	44.29	11.43	13133	0.894	4.78	50.67	16.28	12893	1.512	7.03	85.99	35.74	12847
Caribbean	trades	0.378	1.94	91.55	171.63	2872	0.288	1.87	69.60	122.36	2875	0.327	1.75	79.01	127.74	2875	0.359	1.67	86.99	163.41	2871
Indian Monsoon Gyres	trades	0.674	3.45	43.19	19.98	10282	0.537	3.50	34.45	15.16	10287	0.707	3.78	45.30	21.15	10284	0.783	3.64	50.24	17.11	10270
Indian S Subtrop Gyre	trades	0.997	5.10	57.99	17.54	12392	0.743	4.84	43.21	12.96	12405	0.749	4.01	43.53	13.61	12407	1.076	5.00	62.54	14.20	12400
N Pac Trop Gyre	trades	0.551	2.82	40.67	21.12	9584	0.704	4.58	47.59	12.79	10511	0.773	4.13	51.88	14.32	10586	0.547	2.55	37.74	15.63	10281
N Pac Eq Countercurrent	trades	0.381	1.95	42.66	12.67	5918	0.444	2.89	49.48	17.41	5946	0.476	2.54	53.11	14.07	5929	0.466	2.17	51.95	13.09	5941
Pac Eq Divergence	trades	0.598	3.06	41.33	14.88	9489	0.528	3.43	36.45	10.50	9492	0.594	3.18	41.49	18.14	9385	0.762	3.54	52.85	21.38	9444
W Pac Warm Pool	trades	0.592	3.03	48.14	22.00	8099	0.544	3.54	43.71	13.75	8191	0.619	3.31	49.76	16.53	8190	0.608	2.83	48.89	14.04	8190
Archipelagic Deep Basins	trades	0.528	2.70	57.52	59.00	6294	0.434	2.82	47.03	45.64	6321	0.517	2.77	56.11	58.44	6317	0.523	2.43	56.50	48.20	6340
NE Atl Shelves	coastal	0.065	0.33	675.17	282.83	95	0.111	0.72	174.26	77.71	777	0.087	0.46	141.37	45.53	738	0.003	0.02	252.22	181.41	13
Canary Coastal (EACB)	coastal	0.059	0.30	93.09	79.97	480	0.063	0.41	95.52	53.06	498	0.046	0.25	72.06	45.42	485	0.065	0.30	104.73	85.82	465
Guinea Current Coastal	coastal	0.020	0.10	55.49	31.21	242	0.049	0.32	49.97	53.11	642	0.048	0.26	73.20	46.17	429	0.058	0.27	78.48	42.22	484
Guianas Coastal	coastal	0.188	0.96	155.72	212.66	796	0.139	0.90	112.66	156.04	812	0.164	0.88	135.37	181.30	798	0.217	1.01	176.37	248.78	811
NW Atl Shelves	coastal	0.207	1.06	154.34	179.90	1152	0.180	1.17	86.11	79.16	1877	0.361	1.93	171.46	132.59	1898	0.163	0.76	121.47	123.35	1150
Brazil Current Coastal	coastal	0.061	0.31	61.57	49.07	724	0.073	0.47	73.34	67.17	723	0.085	0.45	85.59	84.24	720	0.078	0.36	78.01	72.97	728
SWR Atl Shelves	coastal	0.153	0.78	117.32	35.28	1311	0.010	0.07	81.09	48.24	112	0.081	0.43	263.26	235.93	278	0.226	1.05	173.56	61.89	1310
Benguela Current Coastal	coastal	0.102	0.52	94.63	49.74	783	0.075	0.49	69.87	26.82	775	0.109	0.58	104.94	35.83	752	0.167	0.78	155.74	56.88	779
E Africa Coastal	coastal	0.246	1.26	69.69	49.41	2565	0.228	1.49	64.65	68.73	2566	0.296	1.58	83.76	96.93	2567	0.298	1.39	84.39	71.31	2568
Red Sea	coastal	0.037	0.19	81.23	85.57	318	0.034	0.22	72.26	68.20	330	0.034	0.18	72.19	67.27	328	0.037	0.17	80.05	67.66	321
Persian Gulf	coastal	0.051	0.26	301.90	220.31	124	0.024	0.16	141.76	67.59	125	0.025	0.13	146.35	77.05	126	0.057	0.26	332.59	259.81	125
NW Arabian Upwelling	coastal	0.169	0.86	49.05	34.83	2322	0.153	0.99	45.43	31.87	2267	0.274	1.47	90.76	47.83	2032	0.218	1.01	63.22	30.41	2325
E India Coastal	coastal	0.074	0.38	82.03	103.51	611	0.090	0.59	99.25	113.17	620	0.137	0.74	159.13	161.75	589	0.092	0.43	124.38	142.15	502
W India Coastal	coastal	0.103	0.53	129.03	183.79	542	0.089	0.58	112.26	184.55	540	0.102	0.54	154.71	208.50	443	0.096	0.45	119.37	170.12	546
Australia West	coastal	0.210	1.07	76.53	79.26	1961	0.269	1.75	97.78	114.53	1965	0.382	2.04	138.01	175.72	1976	0.252	1.17	91.47	92.96	1966

Table 6. (continued)

Int. PIC Over Euphotic Zone		Jan–Mar					Apr–Jun					Jul–Sep					Oct–Dec				
Province	Biome	Tot. PIC, Mt	% Total	Avg Int. PIC, mg/m^2	SD, mg/m^2	Pixels	Tot. PIC, Mt	% Total	Avg Int. PIC, mg/m^2	SD, mg/m^2	Pixels	Tot. PIC, Mt	% Total	Avg Int. PIC, mg/m^2	SD, mg/m^2	Pixels	Tot. PIC, Mt	% Total	Avg Int. PIC, mg/m^2	SD, mg/m^2	Pixels
Alaska Downwelling Coastal	coastal	0.000	0.00	37.22	0.00	2	0.049	0.32	101.31	40.92	562	0.078	0.42	164.69	63.35	554	0.000	0.00	0.00	0.00	0
California Upwelling Coastal	coastal	0.120	0.62	53.97	43.74	1747	0.197	1.28	77.67	34.42	2042	0.215	1.15	79.41	37.07	2166	0.145	0.67	62.17	41.32	1818
Centr American Coastal	coastal	0.089	0.46	76.51	73.73	791	0.091	0.59	78.65	48.26	787	0.109	0.58	95.34	96.33	777	0.106	0.49	91.81	86.07	785
Chile	coastal	0.197	1.01	81.42	36.38	1873	0.154	1.00	74.51	35.90	1517	0.166	0.89	87.23	42.02	1438	0.283	1.32	117.57	42.82	1867
China Sea Coastal	coastal	0.242	1.24	379.29	366.31	471	0.074	0.48	106.22	100.98	514	0.085	0.46	121.68	127.93	520	0.191	0.89	283.81	280.71	498
Sunda	coastal	0.433	2.21	114.41	158.49	2490	0.308	2.00	80.17	114.41	2528	0.378	2.02	98.68	133.73	2524	0.426	1.98	110.85	148.38	2532
E Australian Coastal	coastal	0.064	0.33	61.85	67.83	748	0.053	0.34	51.63	55.79	746	0.061	0.33	59.12	60.72	750	0.063	0.29	61.02	50.91	751
New Zealand Coastal	coastal	0.104	0.53	86.77	41.01	1108	0.044	0.29	111.89	134.35	341	0.059	0.32	90.43	89.01	579	0.146	0.68	121.07	49.51	1110
Unclassified		0.026	0.13	60.37	66.04	347	0.024	0.16	60.35	122.27	307	0.034	0.18	80.47	156.64	327	0.029	0.13	69.07	61.27	324
Summary		**19.546**	**100.00**	**88.40**	**101.21**	**238307**	**15.372**	**100.00**	**85.26**	**113.10**	**209860**	**18.699**	**100.00**	**99.47**	**77.03**	**218750**	**21.501**	**100.00**	**88.21**	**64.95**	**232814**
Polar		**2.408**	**12.32**	**91.35**	**31.85**	**31767**	**1.035**	**6.73**	**103.70**	**30.15**	**14586**	**2.138**	**11.43**	**172.45**	**58.47**	**19733**	**1.578**	**7.34**	**90.58**	**35.58**	**19716**
Westerlies		**7.703**	**39.41**	**66.98**	**38.63**	**95911**	**5.913**	**38.47**	**118.83**	**34.25**	**79786**	**6.580**	**35.19**	**105.97**	**32.59**	**84327**	**9.011**	**41.91**	**74.49**	**31.57**	**99014**
Trades		**6.415**	**32.82**	**50.96**	**44.86**	**87026**	**5.843**	**38.01**	**45.33**	**31.99**	**91515**	**6.567**	**35.12**	**51.76**	**36.34**	**90896**	**7.496**	**34.86**	**57.13**	**40.98**	**90306**
Coastal		**2.994**	**15.32**	**134.27**	**107.17**	**23256**	**2.556**	**16.63**	**89.49**	**77.17**	**23666**	**3.381**	**18.08**	**116.90**	**99.66**	**23467**	**3.387**	**15.75**	**125.41**	**104.67**	**23454**

[a]Provinces are grouped into their respective biome: Polar, Westerlies, Trades, and Coastal. Calculations have been made for each 3 month period of 2002. The algorithm used to estimate POC is described in the text. Results are given for each province for (1) total euphotic zone PIC (essentially, the total PIC found above the 1% light depth of the water column, aerially integrated over the province), (2) average integrated PIC (mg m^{-2}), (3) standard deviation of the average PIC (mg m^{-2}), and (4) the total number of pixels available for the analysis. Any values of 0.00 in the first three columns of the polar biome for each 3 month period represent regions where no satellite radiance data were available, mainly due to low Sun angle. At the bottom of the table the global statistics are provided as well as statistics for each of the four biomes.

period, were boreal polar, Atlantic subarctic, North Pacific epicontinental, Antarctic, Austral Polar, North Atlantic drift, Black Sea, Pacific subarctic gyres (east and west), North Pacific polar front, North Pacific subtropical gyre, South Pacific subtropical gyre, south subtropical convergence, subantarctic, South Atlantic gyre, Indian Monsoon gyres, Indian subtropical gyre, North Pacific tropical gyre, Pacific Equatorial divergence, West Pacific warm pool, and Archipelagic deep basins. Not a single coastal province contributed more than 0.5 Mt PIC in any 3 month period.

[37] We summarize the POC budget as well, in order to support our estimates of the PIC:POC ratios globally. As with the PIC concentrations, the polar POC estimates are likely underestimates due to the fact that remote sensing is limited during winter and fall months of either hemisphere. Average surface POC concentrations were $\sim$40–52 mg m^{-3}, with highest average global POC from April to June (mean for all biomes = 52.1 mg m^{-3}; SD = 26.05 (Table 7)). Provinces with POC concentrations >80 mg m^{-3} (which is $\sim$1.5–2 $\times$ the mean) for at least one 3 month period of the year were Atlantic subarctic, Black Sea, northeast Atlantic shelves, northwest Atlantic shelves, southwest Atlantic shelves, Persian Gulf, Alaska downwelling, and west India coastal waters. As expected, lowest POC concentrations were consistently seen in the subtropical and tropical gyre systems of the Trades and Westerlies biomes. Our results nonetheless demonstrated that the Westerlies and Trades biomes accounted for 80–82% of global POC, even greater than the percentage of global PIC that comes from those same biomes. Polar regimes accounted for only 4.7–8.5% of the global POC, less than the fraction of total global PIC that is produced in the same region (Table 7). Coastal biomes supplied 11.8–13.9% of the global POC. Interestingly, the period from January to March and October to December had the highest global concentrations of POC (699 and 682 Mt, respectively, as opposed to 631 and 647 Mt during April–June and July–September (Table 8)).

[38] The PIC:POC ratio was estimated from the data shown in Tables 5 and 7 (note, because of how the PIC calculations were made, the ratios are identical whether they are based on surface or euphotic integrated estimates; thus, results are only shown in Table 5). The global average PIC:POC ratio varied from 0.041 (April–June) to 0.051 (July–September). Such values are highly consistent with average global export ratios estimated by *Sarmiento et al.* [2002] based on a biogeochemical transport box model of the top 100 m, using measurements of the vertical gradients of potential alkalinity and nitrate. The reader should note that our PIC:POC estimates would not be expected to match PIC:POC export ratios at 100 m. This is mainly because there can be mineralization of both components between the surface optical depth (the top few meters visible to MODIS/Terra [*Gordon and McCluney*, 1975]) and the 100 m depth horizon used by *Sarmiento et al.* [2002]. Nonetheless, their area-weighted global mean export ratio (0.056 $\pm$ 0.004; based on ocean chemistry) was strikingly close to our average global value of 0.047 $\pm$ 0.004 for all seasons, based on MODIS water-leaving radiance measurements.

Table 7. Surface POC Aerially Integrated Within the Biogeochemical Provinces Defined by *Longhurst* [1998][a]

Surface POC		Jan.–Mar				Apr–Jun				Jul–Sep				Oct–Dec			
Province	Biome	Tot. POC, Mt	Avg. Surf. POC, mg/m^3	SD, mg/m^3	Pixels	Tot. POC, Mt	Avg. Surf. POC, mg/m^3	SD, mg/m^3	Pixels	Tot. POC, Mt	Avg. Surf. POC, mg/m^3	SD, mg/m^3	Pixels	Tot. POC, Mt	Avg. Surf. POC, mg/m^3	SD, mg/m^3	Pixels
Boreal Polar	polar	0.0000	0.00	0.00	0	0.1150	78.39	13.79	2786	0.2705	64.46	13.04	7360	0.0000	0.00	0.00	0
Atl Arctic	polar	0.0000	30.52	0.00	1	0.2210	70.59	9.94	4997	0.1914	60.77	8.01	4997	0.0000	0.00	0.00	0
Atl Subarctic	polar	0.0000	0.00	0.00	0	0.1750	87.75	7.78	3227	0.1360	68.16	7.69	3228	0.0000	0.00	0.00	0
N Pac Epicontinental	polar	0.0467	54.63	10.31	784	0.3361	92.31	16.63	4031	0.2587	65.41	8.37	4426	0.0381	56.28	6.15	608
Antarctic	polar	0.7814	38.41	6.00	26816	0.0000	0.00	0.00	0	0.0000	0.00	0.00	0	0.5807	39.67	4.53	18713
Austral Polar	polar	0.2238	57.12	10.55	6370	0.0000	0.00	0.00	0	0.0000	0.00	0.00	0	0.0194	40.97	4.02	719
N Atl Drift(WWDR)	westerlies	0.0730	34.95	5.12	2004	0.2353	66.15	7.89	3612	0.1921	54.03	6.74	3609	0.0506	38.24	2.15	1239
Gulf Stream	westerlies	0.0556	48.78	10.11	977	0.0626	53.86	10.83	996	0.0359	30.95	4.44	996	0.0450	38.87	5.28	994
N Atl Subtrop Gyre (W)	westerlies	0.1711	28.63	5.61	4622	0.1572	26.30	8.98	4622	0.1137	19.02	2.15	4622	0.1426	23.85	3.80	4622
Mediterranean Sea	westerlies	0.1095	42.05	7.73	2130	0.0858	32.94	7.65	2131	0.0689	26.45	4.81	2130	0.0875	33.71	6.55	2124
Black Sea	westerlies	0.0339	86.21	14.54	351	0.0331	83.63	16.01	353	0.0282	71.60	6.71	351	0.0276	71.59	8.59	343
N Atl Subtrop Gyre (E)	westerlies	0.1499	33.79	5.48	3559	0.2001	45.11	16.08	3559	0.1159	26.12	5.26	3559	0.1263	28.47	4.30	3559
Pac Subarctic Gyres (E)	westerlies	0.0607	38.89	2.58	1518	0.1850	56.90	9.73	3371	0.1674	52.81	5.77	3293	0.0307	45.50	3.07	638
Pac Subarctic Gyres (W)	westerlies	0.0846	41.61	3.59	1942	0.1399	64.48	11.23	2105	0.1326	60.01	8.14	2139	0.0629	48.01	5.21	1218
Kuroshio Current	westerlies	0.1360	42.33	12.51	2504	0.1722	53.36	19.93	2517	0.1106	34.41	9.53	2506	0.1215	37.98	9.37	2493
N Pac Polar Front	westerlies	0.2986	40.80	4.87	6214	0.3139	43.82	8.47	6080	0.2301	31.67	5.54	6169	0.2678	36.63	4.55	6207
N Pac Subtrop Gyre	westerlies	0.2915	21.11	6.94	9839	0.2851	20.65	6.35	9839	0.2450	17.75	1.67	9839	0.2725	19.74	3.70	9839
Tasman Sea	westerlies	0.0529	31.31	5.59	1388	0.0786	46.69	4.57	1383	0.0767	45.50	4.48	1384	0.0821	48.57	4.64	1388
S Pac Subtrop Gyre	westerlies	0.6422	17.84	6.88	25907	0.8518	23.67	7.29	25890	0.9172	25.58	6.95	25809	0.7695	21.52	7.73	25743
S Subtrop Convergence	westerlies	0.6278	36.41	11.53	14792	0.6245	42.78	7.14	12363	0.6229	37.20	5.02	14328	0.7104	41.21	7.56	14790
Subantarctic	westerlies	1.2271	39.05	7.87	31554	0.1568	43.90	5.50	3162	0.3122	34.62	3.77	8232	1.3404	42.44	6.33	31734
N Atl Trop Gyre	trades	0.1904	23.60	9.56	5577	0.2137	26.55	15.71	5562	0.1923	23.92	9.77	5557	0.1947	24.13	8.27	5578
W Trop Atl	trades	0.1469	27.26	5.16	3539	0.1874	34.79	7.35	3537	0.1879	34.87	7.96	3539	0.1645	30.52	4.45	3539
East Trop Atl	trades	0.1632	32.34	11.72	3309	0.1965	38.15	10.91	3379	0.2157	42.93	9.67	3295	0.1797	34.87	6.77	3380
S Atl Gyre	trades	0.3581	19.87	6.63	13146	0.5134	28.49	7.84	13146	0.5675	31.86	7.82	13005	0.4965	27.81	11.01	13032
Caribbean	trades	0.1456	35.00	17.07	2891	0.1329	31.98	15.70	2887	0.1338	32.18	14.39	2889	0.1438	34.58	13.86	2891
Indian Monsoon Gyres	trades	0.4192	26.83	6.56	10301	0.4631	29.65	5.47	10298	0.5492	35.17	8.37	10295	0.4651	29.77	5.00	10298
Indian S Subtrop Gyre	trades	0.3051	17.73	3.47	12407	0.4647	27.00	5.34	12407	0.5194	30.18	4.93	12407	0.3876	22.52	4.79	12407
N Pac Trop Gyre	trades	0.3311	22.14	5.11	10622	0.3221	21.69	4.81	10550	0.3053	20.47	2.55	10594	0.3181	21.27	2.79	10625
N Pac Eq Countercurrent	trades	0.2979	33.16	10.20	5948	0.3182	35.42	13.75	5948	0.2643	29.48	7.76	5934	0.2509	27.93	7.96	5947
Pac Eq Divergence	trades	0.4560	31.48	4.84	9492	0.5156	35.59	5.17	9492	0.4967	34.66	5.37	9387	0.4414	30.62	5.50	9444
W Pac Warm Pool	trades	0.2483	19.96	5.52	8188	0.2732	21.95	5.45	8191	0.2686	21.58	4.48	8191	0.2624	21.08	3.91	8191
Archipelagic Deep Basins	trades	0.2509	27.07	15.44	6348	0.2896	31.25	11.64	6347	0.3276	35.39	10.07	6340	0.2674	28.82	11.21	6356
NE Atl Shelves	coastal	0.0086	73.77	11.68	115	0.0848	130.27	18.50	795	0.0578	88.37	17.50	800	0.0012	48.44	9.17	23
Canary Coastal (EACB)	coastal	0.0509	76.44	32.91	502	0.0634	95.40	52.60	501	0.0351	54.22	23.23	490	0.0354	53.32	20.43	501
Guinea Current Coastal	coastal	0.0462	57.43	22.72	531	0.0605	60.87	21.35	655	0.0360	51.21	12.92	462	0.0503	51.40	15.47	645
Guianas Coastal	coastal	0.0744	59.59	63.03	823	0.0933	73.71	71.01	834	0.0795	62.92	61.17	833	0.0732	57.45	58.78	840
NW Atl Shelves	coastal	0.1089	64.92	20.52	1469	0.1754	82.83	22.73	1908	0.1226	57.81	16.87	1911	0.0849	56.77	17.10	1289
Brazil Current Coastal	coastal	0.0387	38.71	23.11	730	0.0425	42.61	15.50	727	0.0431	43.29	17.65	726	0.0420	42.08	25.12	728
SW Atl Shelves	coastal	0.1208	92.42	28.17	1315	0.0104	75.07	12.32	122	0.0238	62.72	13.01	347	0.1137	87.05	25.11	1315
Benguela Current Coastal	coastal	0.0778	72.05	48.78	783	0.0847	78.39	31.23	783	0.0695	66.03	18.15	764	0.0778	72.32	25.58	780
E Africa Coastal	coastal	0.1229	34.77	21.06	2568	0.1618	45.81	16.29	2567	0.1570	44.43	11.91	2568	0.1324	37.45	14.19	2569
Red Sea	coastal	0.0244	50.32	21.26	339	0.0205	41.84	16.35	343	0.0188	38.73	14.04	340	0.0237	48.51	16.63	342
Persian Gulf	coastal	0.0171	100.21	12.56	125	0.0147	86.25	9.33	125	0.0111	64.49	7.84	126	0.0131	75.94	8.43	126
NW Arabian Upwelling	coastal	0.2196	63.37	20.17	2337	0.1576	45.59	21.66	2331	0.2079	65.31	19.78	2141	0.1808	52.16	14.98	2337
E India Coastal	coastal	0.0571	58.91	49.50	662	0.0541	57.63	44.01	640	0.0482	54.70	29.39	601	0.0562	57.57	47.16	666
W India Coastal	coastal	0.0663	78.54	52.77	575	0.0597	71.60	51.30	567	0.0563	82.55	38.51	460	0.0590	69.85	40.80	575
Australia West	coastal	0.0942	34.04	14.26	1978	0.1295	46.80	13.49	1976	0.1281	46.23	11.40	1979	0.1019	36.89	11.59	1974

Table 7. (continued)

Surface POC		Jan.–Mar				Apr–Jun				Jul–Sep				Oct–Dec			
Province	Biome	Tot. POC, Mt	Avg. Surf. POC, mg/m^3	SD, mg/m^3	Pixels	Tot. POC, Mt	Avg. Surf. POC, mg/m^3	SD, mg/m^3	Pixels	Tot. POC, Mt	Avg. Surf. POC, mg/m^3	SD, mg/m^3	Pixels	Tot. POC, Mt	Avg. Surf. POC, mg/m^3	SD, mg/m^3	Pixels
Alaska Downwelling Coastal	coastal	0.0006	54.01	6.22	11	0.0572	117.35	13.99	569	0.0378	78.91	6.89	559	0.0000	0.00	0.00	0
California Upwelling Coastal	coastal	0.1266	47.13	19.62	2144	0.1477	57.40	30.78	2070	0.1225	45.16	19.78	2172	0.1040	42.39	13.48	1914
Centr American Coastal	coastal	0.0784	67.08	27.84	794	0.0749	64.55	26.84	789	0.0528	45.90	18.62	782	0.0584	50.27	19.41	790
Chile	coastal	0.1486	60.80	28.69	1891	0.1437	69.33	26.52	1522	0.1100	56.62	15.48	1469	0.1442	59.66	19.91	1874
China Sea Coastal	coastal	0.0553	79.13	29.15	518	0.0446	63.73	24.00	519	0.0352	50.27	13.55	520	0.0418	59.92	20.07	517
Sunda	coastal	0.1606	41.80	17.69	2531	0.1600	41.27	14.91	2554	0.1596	41.38	13.06	2541	0.1498	38.71	12.85	2549
East Australian Coastal	coastal	0.0260	25.14	7.09	754	0.0355	34.32	7.52	753	0.0380	36.62	6.65	754	0.0305	29.41	9.50	755
New Zealand Coastal	coastal	0.0563	46.67	9.51	1112	0.0253	55.27	6.08	396	0.0361	44.69	5.46	721	0.0632	52.48	9.93	1110
Unclassified		0.0136	30.61	24.31	360	0.0154	37.74	37.86	318	0.0149	34.70	28.70	337	0.0123	29.31	15.57	327
Summary		**10.1730**	**43.66**	**21.56**	**260007**	**10.2363**	**52.13**	**26.05**	**213132**	**9.9558**	**44.15**	**18.76**	**224813**	**9.9977**	**39.59**	**18.56**	**243205**
Polar		**1.052**	**50.05**	**8.95**	**33970**	**0.847**	**82.26**	**12.03**	**15041**	**0.857**	**64.70**	**9.28**	**20011**	**0.638**	**45.64**	**4.90**	**20040**
Westerlies		**4.014**	**38.92**	**7.40**	**109301**	**3.582**	**46.95**	**9.84**	**81983**	**3.369**	**37.85**	**5.40**	**88966**	**4.137**	**38.42**	**5.52**	**106931**
Trades		**3.313**	**26.37**	**8.44**	**91768**	**3.890**	**30.21**	**9.10**	**91744**	**4.028**	**31.06**	**7.76**	**91433**	**3.572**	**27.83**	**7.13**	**91688**
Coastal		**1.780**	**59.88**	**25.58**	**24607**	**1.902**	**66.87**	**24.71**	**24046**	**1.687**	**55.76**	**17.95**	**24066**	**1.638**	**51.31**	**19.81**	**24219**

[a]Provinces are grouped into their respective biome: Polar, Westerlies, Trades, and Coastal. Calculations have been made for each 3 month period of 2002. The algorithm used to derive POC concentrations was according to *Morel* [1988] and is described in the text. Results are given for each province for (1) total POC (essentially, the total POC found in the top meter of the water column, aerially integrated over the province), (2) average surface POC (mg m^{-3}), (3) standard deviation of the average POC (mg m^{-3}), and (4) the total number of pixels available for the analysis. Any values of 0.00 in the first three columns of the polar biome for each 3 month period represent regions where no satellite radiance data were available, mainly due to low Sun angle. At the bottom of the table global statistics are provided as well as statistics for each of the four biomes.

Table 8. Euphotic Zone POC Aerially Integrated Within the Biogeochemical Provinces Defined by *Longhurst* [1998][a]

Int. POC Over Euphotic Zone		Jan–Mar					Apr–Jun					Jul–Sep					Oct–Dec				
Province	Biome	Int. POC, Mt	% Total	Avg. Int. POC, mg/m^2	SD, mg/m^2	Pixels	Int. POC, Mt	% Total	Avg. Int. POC, mg/m^2	SD, mg/m^2	Pixels	Int. POC, Mt	% Total	Avg. Int. POC, mg/m^2	SD, mg/m^2	Pixels	Int. POC, Mt	% Total	Avg. Int. POC, mg/m^2	SD, mg/m^2	Pixels
Boreal Polar	polar	0.000	0.00	0.00	0.00	0	4.158	0.66	2834.36	362.72	2786	11.269	1.74	2685.57	318.29	7360	0.000	0.00	0.00	0.00	0
Atl Arctic	polar	0.002	0.00	2200.79	0.00	1	8.661	1.37	2766.42	318.65	4997	8.379	1.29	2660.96	309.57	4997	0.000	0.00	0.00	0.00	0
Atl Subarctic	polar	0.000	0.00	0.00	0.00	0	5.867	0.93	2941.31	207.45	3227	5.475	0.85	2743.88	219.98	3228	0.000	0.00	0.00	0.00	0
N Pac Epicontinental	polar	2.202	0.31	2575.12	195.71	784	10.812	1.71	2969.20	264.13	4031	10.705	1.65	2706.74	187.26	4426	1.764	0.26	2604.19	112.39	608
Antarctic	polar	47.352	6.77	2327.40	141.38	26816	0.000	0.00	0.00	0.00	0	0.000	0.00	0.00	0.00	0	34.552	5.07	2360.06	140.46	18713
Austral Polar	polar	10.075	1.44	2571.39	146.14	6370	0.000	0.00	0.00	0.00	0	0.000	0.00	0.00	0.00	0	1.125	0.17	2375.89	151.20	719
N Atl Drift(WWDR)	westerlies	4.754	0.68	2277.60	110.42	2004	9.687	1.53	2722.87	162.41	3612	9.122	1.41	2566.18	107.90	3609	3.101	0.45	2341.62	42.36	1239
Gulf Stream	westerlies	2.836	0.41	2487.58	133.55	977	2.967	0.47	2555.10	117.31	996	2.555	0.39	2200.44	64.42	996	2.718	0.40	2345.24	64.92	994
N Atl Subtrop Gyre (W)	westerlies	12.824	1.83	2145.67	87.93	4622	12.410	1.97	2076.44	126.68	4622	11.499	1.78	1924.04	32.44	4622	12.218	1.79	2044.41	44.98	4622
Mediterranean Sea	westerlies	6.226	0.89	2391.37	92.36	2130	5.806	0.92	2228.89	104.68	2131	5.475	0.85	2103.04	80.70	2130	5.839	0.86	2248.71	98.74	2124
Black Sea	westerlies	1.152	0.16	2927.53	130.01	351	1.148	0.18	2899.48	151.30	353	1.097	0.17	2786.85	79.51	351	1.072	0.16	2784.57	103.67	343
N Atl Subtrop Gyre (E)	westerlies	9.991	1.43	2251.75	104.81	3559	10.620	1.68	2393.36	152.53	3559	9.279	1.43	2091.20	83.51	3559	9.523	1.40	2146.32	65.90	3559
Pac Subarctic Gyres (E)	westerlies	3.671	0.52	2351.89	58.68	1518	8.438	1.34	2594.78	96.42	3371	8.097	1.25	2553.92	105.87	3293	1.660	0.24	2457.34	58.64	638
Pac Subarctic Gyres (W)	westerlies	4.871	0.70	2395.83	91.57	1942	5.849	0.93	2696.34	152.12	2105	5.846	0.90	2645.96	123.38	2139	3.265	0.48	2492.00	91.94	1218
Kuroshio Current	westerlies	7.600	1.09	2365.41	157.37	2504	8.046	1.27	2492.88	179.03	2517	7.213	1.11	2243.09	120.00	2506	7.381	1.08	2306.48	109.82	2493
N Pac Polar Front	westerlies	17.427	2.49	2381.34	114.89	6214	17.321	2.74	2418.31	136.65	6080	16.057	2.48	2209.56	75.06	6169	16.870	2.47	2307.61	82.79	6207
N Pac Subtrop Gyre	westerlies	27.011	3.86	1956.54	117.82	9839	26.932	4.27	1950.78	92.49	9839	26.083	4.03	1889.33	55.73	9839	26.764	3.92	1938.64	53.97	9839
Tasman Sea	westerlies	3.725	0.53	2204.69	88.35	1388	4.163	0.66	2472.71	61.30	1383	4.139	0.64	2456.94	95.75	1384	4.223	0.62	2499.88	60.37	1388
S Pac Subtrop Gyre	westerlies	67.186	9.61	1866.10	243.41	25907	73.060	11.58	2030.29	202.65	25890	74.457	11.50	2076.38	187.99	25809	70.358	10.32	1967.25	224.94	25743
S Subtrop Convergence	westerlies	39.157	5.60	2271.23	176.10	14792	35.102	5.56	2404.58	109.12	12363	38.827	6.00	2318.79	111.65	14328	40.987	6.01	2377.68	130.35	14790
Subantarctic	westerlies	73.553	10.52	2340.87	175.85	31554	8.672	1.37	2428.46	88.73	3162	20.520	3.17	2275.31	85.27	8232	75.861	11.13	2402.09	155.44	31734
N Atl Trop Gyre	trades	16.325	2.33	2023.40	200.95	5577	16.637	2.64	2067.60	277.55	5562	16.331	2.52	2031.45	202.93	5557	16.488	2.42	2043.22	179.40	5578
W Trop Atl	trades	11.463	1.64	2126.85	91.26	3539	12.253	1.94	2274.75	111.82	3537	12.253	1.89	2273.42	136.64	3539	11.837	1.74	2196.31	84.31	3539
East Trop Atl	trades	11.165	1.60	2213.09	197.42	3309	11.983	1.90	2325.84	165.61	3379	12.099	1.87	2407.98	153.17	3295	11.728	1.72	2275.68	120.60	3380
S Atl Gyre	trades	34.728	4.97	1926.99	149.06	13146	38.472	6.10	2134.73	136.81	13146	39.309	6.07	2206.85	150.14	13005	37.503	5.50	2100.67	199.98	13032
Caribbean	trades	9.343	1.34	2246.15	214.81	2891	9.113	1.44	2193.64	224.33	2887	9.154	1.41	2202.00	216.70	2889	9.360	1.37	2250.26	186.95	2891
Indian Monsoon Gyres	trades	32.992	4.72	2111.54	141.06	10301	33.997	5.39	2176.50	103.04	10298	35.558	5.49	2277.07	142.64	10295	34.046	4.99	2179.67	102.86	10298
Indian S Subtrop Gyre	trades	32.411	4.63	1883.55	123.46	12407	36.399	5.77	2115.35	116.30	12407	37.615	5.81	2185.97	122.26	12407	34.590	5.07	2010.21	121.07	12407
N Pac Trop Gyre	trades	29.898	4.27	1999.56	117.78	10622	29.575	4.69	1991.43	140.03	10550	29.321	4.53	1966.22	106.70	10594	29.711	4.36	1986.46	101.01	10625
N Pac Eq Countercurrent	trades	20.063	2.87	2233.18	174.36	5948	20.405	3.23	2271.23	193.02	5948	19.406	3.00	2165.19	154.10	5934	19.134	2.81	2130.06	158.90	5947
Pac Eq Divergence	trades	32.087	4.59	2215.16	87.95	9492	33.209	5.26	2292.66	86.89	9492	32.590	5.03	2274.51	100.38	9387	31.639	4.64	2195.06	113.87	9444
W Pac Warm Pool	trades	24.151	3.45	1941.19	155.11	8188	24.847	3.94	1996.41	140.49	8191	24.767	3.83	1989.97	121.80	8191	24.634	3.61	1979.25	106.55	8191
Archipelagic Deep Basins	trades	19.379	2.77	2090.99	270.60	6348	20.355	3.23	2196.63	190.29	6347	21.084	3.26	2277.89	176.77	6340	19.907	2.92	2145.13	206.43	6356
NE Atl Shelves	coastal	0.327	0.05	2796.14	129.12	115	2.128	0.34	3270.12	216.09	795	1.907	0.29	2916.59	209.70	800	0.060	0.01	2484.89	112.29	23
Canary Coastal (EACB)	coastal	1.859	0.27	2793.26	431.66	502	1.941	0.31	2922.04	594.61	501	1.643	0.25	2534.72	355.80	490	1.682	0.25	2532.84	339.31	501
Guinea Current Coastal	coastal	2.080	0.30	2586.17	268.46	531	2.620	0.42	2636.38	239.51	655	1.775	0.27	2525.54	170.32	462	2.468	0.36	2522.80	191.04	645
Guianas Coastal	coastal	3.076	0.44	2463.86	572.99	823	3.328	0.53	2630.68	591.45	834	3.205	0.50	2536.05	527.53	833	3.140	0.46	2464.00	524.20	840
NW Atl Shelves	coastal	4.485	0.64	2673.03	254.01	1469	6.026	0.95	2845.67	213.02	1908	5.470	0.84	2580.15	207.92	1911	3.855	0.57	2577.25	212.70	1289
Brazil Current Coastal	coastal	2.265	0.32	2262.93	228.12	730	2.358	0.37	2365.56	183.62	727	2.358	0.36	2368.91	231.98	726	2.300	0.34	2304.64	245.52	728
SW Atl Shelves	coastal	3.844	0.55	2941.61	316.87	1315	0.389	0.06	2815.05	143.36	122	1.013	0.16	2668.73	181.73	347	3.789	0.56	2900.22	316.48	1315
Benguela Current Coastal	coastal	2.874	0.41	2661.00	506.24	783	3.037	0.48	2811.76	340.01	783	2.849	0.44	2707.85	246.10	764	2.971	0.44	2762.49	288.90	780
E Africa Coastal	coastal	7.855	1.12	2222.48	277.05	2568	8.596	1.36	2433.30	206.65	2567	8.571	1.32	2425.24	178.82	2568	8.112	1.19	2294.32	188.21	2569
Red Sea	coastal	1.207	0.17	2492.32	292.63	339	1.161	0.18	2370.48	272.69	343	1.128	0.17	2324.09	252.56	340	1.210	0.18	2477.71	258.50	342
Persian Gulf	coastal	0.523	0.07	3058.40	106.92	125	0.502	0.08	2934.34	85.93	125	0.466	0.07	2705.66	97.06	126	0.488	0.07	2832.25	85.84	126
NW Arabian Upwelling	coastal	9.243	1.32	2666.56	193.04	2337	8.374	1.33	2422.13	242.06	2331	8.579	1.33	2695.33	197.42	2141	8.788	1.29	2535.68	152.04	2337
E India Coastal	coastal	2.448	0.35	2524.15	416.26	662	2.367	0.38	2522.44	393.75	640	2.231	0.34	2531.68	289.60	601	2.456	0.36	2517.41	395.78	666
W India Coastal	coastal	2.317	0.33	2742.57	432.23	575	2.234	0.35	2680.41	434.88	567	1.938	0.30	2844.00	351.56	460	2.275	0.33	2693.67	346.93	575
Australia West	coastal	6.187	0.88	2235.10	288.35	1978	6.800	1.08	2457.30	248.09	1976	6.808	1.05	2457.28	241.62	1979	6.355	0.93	2299.92	257.84	1974

Table 8. (continued)

Int. POC Over Euphotic Zone		Jan–Mar					Apr–Jun					Jul–Sep					Oct–Dec				
Province	Biome	Int. POC, Mt	% Total	Avg. Int. POC, mg/m^2	SD, mg/m^2	Pixels	Int. POC, Mt	% Total	Avg. Int. POC, mg/m^2	SD, mg/m^2	Pixels	Int. POC, Mt	% Total	Avg. Int. POC, mg/m^2	SD, mg/m^2	Pixels	Int. POC, Mt	% Total	Avg. Int. POC, mg/m^2	SD, mg/m^2	Pixels
Alaska Downwelling Coastal	coastal	0.027	0.00	2572.55	82.46	11	1.554	0.25	3187.39	151.60	569	1.372	0.21	2860.84	121.89	559	0.000	0.00	0.00	0.00	0
California Upwelling Coastal	coastal	6.516	0.93	2426.11	274.22	2144	6.500	1.03	2526.50	336.60	2070	6.489	1.00	2392.06	256.15	2172	5.814	0.85	2369.83	176.90	1914
Centr American Coastal	coastal	3.145	0.45	2692.80	267.21	794	3.096	0.49	2667.76	261.05	789	2.803	0.43	2437.73	216.38	782	2.903	0.43	2498.29	220.68	790
Chile	coastal	6.372	0.91	2607.76	440.91	1891	5.665	0.90	2733.11	395.90	1522	5.045	0.78	2597.59	329.68	1469	6.338	0.93	2621.48	372.01	1874
China Sea Coastal	coastal	1.959	0.28	2805.53	249.29	518	1.845	0.29	2637.65	221.05	519	1.755	0.27	2502.63	176.49	520	1.821	0.27	2611.67	218.59	517
Sunda	coastal	9.101	1.30	2368.44	227.27	2531	9.191	1.46	2370.54	193.18	2554	9.167	1.42	2376.30	174.24	2541	9.020	1.32	2331.11	173.00	2549
East Australian Coastal	coastal	2.136	0.31	2061.66	116.23	754	2.332	0.37	2253.84	95.91	753	2.384	0.37	2299.98	74.52	754	2.225	0.33	2144.41	110.25	755
New Zealand Coastal	coastal	2.967	0.42	2458.43	177.49	1112	1.185	0.19	2591.12	86.56	396	1.973	0.30	2443.12	124.81	721	3.068	0.45	2547.11	201.79	1110
Unclassified		0.948	0.14	2127.81	358.39	360	0.912	0.14	2234.12	437.31	318	0.942	0.15	2198.27	393.83	337	0.893	0.13	2128.84	279.66	327
Summary		**699.380**	**100.00**	**2290.22**	**522.24**	**260007**	**631.105**	**100.00**	**2407.60**	**555.00**	**213132**	**647.453**	**100.00**	**2321.53**	**511.77**	**224813**	**681.892**	**100.00**	**2192.01**	**648.06**	**243205**
Polar		**59.630**	**8.53**	**2491.30**	**161.07**	**33970**	**29.497**	**4.67**	**2877.82**	**288.24**	**15041**	**35.827**	**5.53**	**2699.29**	**258.77**	**20011**	**37.442**	**5.49**	**2446.71**	**134.68**	**20040**
Westerlies		**281.983**	**40.32**	**2307.69**	**125.54**	**109301**	**230.222**	**36.48**	**2424.35**	**128.90**	**81983**	**240.267**	**37.11**	**2289.40**	**93.95**	**88966**	**281.840**	**41.33**	**2310.66**	**92.59**	**106931**
Trades		**274.006**	**39.18**	**2084.30**	**160.32**	**91768**	**287.246**	**45.51**	**2169.73**	**157.18**	**91744**	**289.488**	**44.71**	**2188.21**	**148.69**	**91433**	**280.577**	**41.15**	**2124.33**	**140.16**	**91688**
Coastal		**82.811**	**11.84**	**2570.12**	**284.74**	**24607**	**83.229**	**13.19**	**2655.89**	**267.29**	**24046**	**80.930**	**12.50**	**2553.57**	**226.69**	**24066**	**81.140**	**11.90**	**2405.39**	**234.30**	**24219**

[a]Provinces are grouped into their respective biome: Polar, Westerlies, Trades, and Coastal. Calculations have been made for each 3 month period of 2002. Results are given for each province for (1) total euphotic zone POC (essentially, the total POC found above the 1% light depth of the water column, aerially integrated over the province), (2) average integrated POC (mg m^{-2}), (3) standard deviation of the average POC (mg m^{-2}), and (4) the total number of pixels available for the analysis. Any values of 0.00 in the first three columns of the polar biome for each 3 month period represent regions where no satellite radiance data were available, mainly due to low Sun angle. At the bottom of the table the global statistics are provided as well as statistics for each of the four biomes.

Note, while these PIC:POC and export ratios are consistent, they are both considerably less than the often-used value of 0.25 (see *Sarmiento et al.* [2002] for further discussion about this discrepancy).

[39] *Sarmiento et al.* [2002] further found their predicted export ratios to be everywhere less than 0.1. This was not true in our case; the highest PIC:POC ratios that we observed (exceeding 0.1 (see Table 5)) were observed in the Black Sea, NE Atlantic shelves, SW Atlantic shelves, Persian Gulf and China Sea Coastal provinces. All Northern Hemisphere polar provinces had PIC:POC ratios >0.05 from July to September. Other provinces with PIC:POC ratios >0.05 for at least one 3 month period were North Atlantic Drift, Black Sea, northeast Atlantic Shelves, Guianas coastal, northwest Atlantic shelves, southwest Atlantic shelves, Benguela Current coastal, Persian Gulf, east India Coastal, west India coastal, Australia West, China Sea coastal, and New Zealand coastal provinces. Regions where our PIC:POC ratios were less than the export ratios of *Sarmiento et al.* [2002] were in the Equatorial regions of the Pacific, Atlantic and Indian Oceans. Moreover, we found higher values of PIC:POC in the North Atlantic subarctic gyre (summer values of 0.093 (Table 5)), compared to export ratios of 0.023 ± 0.02 [*Sarmiento et al.*, 2002]. The reason for this disparity is not immediately obvious, unless calcite dissolution in the top 100 m is responsible for remineralizing a larger proportion of the PIC than POC [*Milliman et al.*, 1999]. Given the frequent blooms in the North Atlantic subarctic gyre, higher PIC concentrations (Tables 5 and 6) and higher PIC:POC ratios clearly would be expected.

[40] Another cross check of the above PIC estimates is to estimate the rate of global PIC turnover in the sea by dividing the average global, MODIS-derived PIC value (18.8 Mt PIC ± 2.56) by the typical annual global calcification rate of ~1 Gt PIC yr^{-1} [*Archer and Maier-Reimer*, 1994; *Archer*, 1997; *Milliman et al.*, 1999; *Morse and Mackenzie*, 1990; *Wollast*, 1994] which gives a quotient of 0.0188 years (= 6.86 days). This value is reasonably consistent with the average turnover time of PIC particles based on direct shipboard measurements of ^{14}C calcification, combined with atomic absorption analyses of PIC standing stock. For example, in the equatorial Pacific, the PIC turnover time typically was ~6.5 days (±3.5 days) [*Balch and Kilpatrick*, 1996] while in the Arabian Sea, the mean turnover time was ~13 days (±6 days), depending on season [*Balch et al.*, 2000]. While these observations reveal internal consistencies between PIC standing stock and field measurements of PIC turnover, one must remember that the turnover time of PIC particles can be highly variable due to factors such as growth and grazing. Moreover, there are few field observations of PIC turnover available to constrain global models of the calcium carbonate cycle. Verification of the global PIC estimates must await further in situ validation measurements from ship. Specifically, the large PIC-rich features observed by the MODIS sensors in the southern ocean, must be verified, as they have a large effect on the total global PIC standing stock.

[41] **Acknowledgments.** Katherine Kilpatrick (University of Miami) helped with algorithm implementation and acquisition of PIC data from several cruises. Amanda Ashe and Jennifer Fritz also provided assistance with some of the validation activities. We gratefully acknowledge several

sources of funding over the years. Primary support was generously provided by NASA (NAS5-31363). Support for algorithm development and validation activities also was provided by NASA (NAGW2426; NAS5-97268; NAG5-10622; NASA EPSCOR EP-02-14), the Office of Naval Research (ONR N00014-91-J-1048, N00014-97-1-0034; N00014-98-1-0882; N00014-99-1-0645; N00014-01-1-0042), the National Science Foundation (OCE-9022227; OCE-9596167; OCE-0136541), and NOAA (NA56RM0258; 40-AA-NE-005996).

References

Ackleson, S., W. M. Balch, and P. M. Holligan (1988), White waters of the Gulf of Maine, *Oceanography*, *1*, 18–22.

Ackleson, S., W. M. Balch, and P. M. Holligan (1994), Response of water-leaving radiance to particulate calcite and chlorophyll a concentrations: A model for Gulf of Maine coccolithophore blooms, *J. Geophys. Res.*, *99*, 7483–7499.

Archer, D. E. (1997), A data-driven model of the global calcite lysocline, *Global Biogeochem. Cycles*, *10*, 511–526.

Archer, D., and E. Maier-Reimer (1994), Effect of deep-sea sedimentary calcite on preservation on atmospheric CO_2 concentration, *Nature*, *367*, 260–263.

Archer, D., H. Kheshgi, and E. Maier-Reimer (1998), Dynamics of fossil fuel CO_2 neutralization by marine $CaCO_3$, *Global Biogeochem. Cycles*, *12*, 259–276.

Armstrong, R. A., C. Lee, J. I. Hedges, S. Honjo, and S. G. Wakeham (2002), A new, mechanistic model for organic carbon fluxes in the ocean based on the quantitative association of POC with ballast minerals, *Deep Sea Res., Part II*, *49*, 219–236.

Balch, W. (1991), Erratum, *Limnol. Oceanogr*, *36*, 1462.

Balch, W. (2001), Validation of surface bio-optical properties in the Gulf of Maine as a means for improving satellite primary production estimates, in *SIMBIOS Project 2000 Annual Report*, edited by G. S. Fargion and C. R. McClain, pp. 26–33, NASA Goddard Space Flight Cent., Greenbelt, Md.

Balch, W. M. (2004), Re-evaluation of the physiological ecology of coccolithophores, in *Coccolithophores: From Molecular Processes to Global Impact*, edited by H. R. Thierstein and J. R. Young, pp. 165–190, Springer, New York.

Balch, W. M., and D. T. Drapeau (2004), Backscattering by coccolithophorids and coccoliths: Sample preparation, measurement and analysis protocols, in *Ocean Optics Protocols For Satellite Ocean Color Sensor Validation, Revision 5: Biogeochemical and Bio-Optical Measurements and Data Analysis Protocols*, edited by J. L. Mueller, G. S. Fargion, and C. R. McClain, pp. 27–36, NASA Goddard Space Flight Space Cent., Greenbelt, Md.

Balch, W. M., and K. A. Kilpatrick (1996), Calcification rates in the equatorial Pacific along 140°W, *Deep Sea Res., Part II*, *43*, 971–993.

Balch, W. M., R. W. Eppley, M. R. Abbott, and F. M. H. Reid (1989), Bias in satellite-derived pigment measurements due to coccolithophores and dinoflagellates, *J. Plankton Res.*, *11*, 575–581.

Balch, W. M., P. M. Holligan, S. G. Ackleson, and K. J. Voss (1991), Biological and optical properties of mesoscale coccolithophore blooms in the Gulf of Maine, *Limnol. Oceanogr.*, *36*, 629–643.

Balch, W. M., P. M. Holligan, and K. A. Kilpatrick (1992), Calcification, photosynthesis and growth of the bloom-forming coccolithophore, *Emiliania huxleyi*, *Cont. Shelf Res.*, *12*, 1353–1374.

Balch, W. M., K. Kilpatrick, P. M. Holligan, D. Harbour, and E. Fernandez (1996a), The 1991 coccolithophore bloom in the central north Atlantic. II, Relating optics to coccolith concentration, *Limnol. Oceanogr.*, *41*, 1684–1696.

Balch, W. M., K. A. Kilpatrick, P. M. Holligan, and C. Trees (1996b), The 1991 coccolithophore bloom in the central north Atlantic. I. Optical properties and factors affecting their distribution, *Limnol. Oceanogr.*, *41*, 1669–1683.

Balch, W. M., D. T. Drapeau, T. L. Cucci, R. D. Vaillancourt, K. A. Kilpatrick, and J. J. Fritz (1999), Optical backscattering by calcifying algae: Separating the contribution by particulate inorganic and organic carbon fractions, *J. Geophys. Res.*, *104*, 1541–1558.

Balch, W. M., D. Drapeau, and J. Fritz (2000), Monsoonal forcing of calcification in the Arabian Sea, *Deep Sea Res., Part II*, *47*, 1301–1337.

Balch, W. M., D. Drapeau, J. Fritz, B. Bowler, and J. Nolan (2001), Optical backscattering in the Arabian Sea: Continuous underway measurements of particulate inorganic and organic carbon, *Deep Sea Res., Part I*, *48*, 2423–2452.

Balch, W. M., D. T. Drapeau, B. C. Bowler, E. S. Booth, J. I. Goes, A. Ashe, and J. M. Frye (2004), A multi-year record of hydrographic and bio-optical properties in the Gulf of Maine: I. Spatial and temporal variability, *Prog. Oceanogr.*, *63*, 57–98.

Bates, N. R., A. F. Michaels, and A. H. Knapp (1996), Alkalinity changes in the Sargasso Sea: Geochemical evidence of calcification?, *Mar. Chem.*, *51*, 347–358.

Berge, G. (1962), Discoloration of the sea due to *Coccolithus huxleyi* "bloom," *Sarsia*, *6*, 27–40.

Birkenes, E., and T. Braarud (1952), Phytoplankton in the Oslo fjord during a "*Coccolithus huxleyi* summer," *Oslo I. Mat. Naturv. Kl.*, *2*, 1–23.

Blackburn, S., and G. Cresswell (1993), A coccolithophorid bloom in Jervis Bay, Australia, *Aust. J. Freshwater Res.*, *44*, 253–260.

Boyle, E. A. (1988), The role of vertical chemical fractionation in controlling late Quaternary atmospheric carbon dioxide, *J. Geophys. Res.*, *93*, 15,701–15,714.

Broecker, W. S., and T.-H. Peng (1982), *Tracers in the Sea*, 660 pp., Lamont-Doherty Geol. Obs. Columbia Univ., Palisades, New York.

Broecker, W. S., and T.-H. Peng (1989), The cause of the glacial to interglacial atmospheric CO_2 change: A polar alkalinity hypothesis, *Global Biogeochem. Cycles*, *3*, 215–239.

Broecker, W. S., and T. Takahashi (1977), Neutralization of fossil fuel CO_2 by marine calcium carbonate, in *The Fate of Fossil CO_2 in the Oceans*, edited by N. R. Anderson and A. Malahoff, pp. 213–241, Springer, New York.

Broerse, A. T. C., T. Tyrrell, J. R. Young, A. J. Poulton, A. Merico, and W. M. Balch (2003), The cause of bright waters in the Bering Sea in winter, *Cont. Shelf Res.*, *23*, 1579–1596.

Brown, C. W., and J. A. Yoder (1994), Coccolithophorid blooms in the global ocean, *J. Geophys. Res.*, *99*, 7467–7482.

Brussaard, C. P. D., R. S. Kempers, A. J. Kop, R. Riegmen, and M. Heldal (1996), Virus-like particles in a summer bloom of *Emiliania huxleyi* in the North Sea, *Aquat. Microbial Ecol.*, *10*, 105–113.

Brzezinski, M. A., D. M. Nelson, V. M. Franck, and D. E. Sigmon (2001), Silicon dynamics within an intense open-ocean diatom bloom in the Pacific sector of the Southern Ocean, *Deep Sea Res., Part II*, *48*, 3997–4018.

Buitenhuis, E., J. van Bleijswijk, D. Bakker, and M. Veldhuis (1996), Trends in inorganic and organic carbon in a bloom of *Emiliania huxleyi* in the North Sea, *Mar. Ecol. Prog. Ser.*, *143*, 271–282.

Burkill, P. H., S. D. Archer, C. Robinson, P. D. Nightingale, S. B. Groom, G. A. Tarran, and M. V. Zubkov (2002), Dimethyl sulphide biogeochemistry within a coccolithophore bloom (DISCO): An overview, *Deep Sea Res., Part II*, *49*, 2863–2885.

Charlson, R. J., J. E. Lovelock, M. O. Andreae, and S. G. Warren (1987), Oceanic phytoplankton, atmospheric sulphur, cloud albedo and climate, *Nature*, *326*, 655–661.

Clark, D. K. (1981), Phytoplankton algorithms for the Nimbus-7 CZCS, in *Oceanography From Space*, edited by J. R. F. Gower, pp. 227–237, Springer, New York.

Cokacar, E. A. (2001), Structure of *Emiliania huxleyi* blooms in the Black Sea surface waters as detected by SeaWIFS imagery, *Geophys. Res. Lett.*, *28*, 4607–4610.

Cullen, J. J. (1990), On models of growth and photosynthesis in phytoplankton, *Deep Sea Res., Part A*, *37*, 667–683.

Eppley, R. W., W. G. Harrison, S. Chisholm, and E. Stewart (1977), Particulate organic matter in surface waters off southern California and its relationship to phytoplankton, *J. Mar. Res.*, *35*, 671–696.

Fagerbakke, K. M., M. Heldal, S. Norland, B. R. Heimdal, and H. Batvik (1994), *Emiliania huxleyi*: Chemical composition and size of coccoliths from enclosure experiments and a Norwegian fjord, *Sarsia*, *79*, 349–355.

Feely, R. A., C. L. Sabine, K. Lee, W. Berelson, J. Kleypas, V. J. Fabry, and F. J. Millero (2004), Impact of anthropogenic CO_2 on the $CaCO_3$ system in the oceans, *Science*, *305*, 362–366.

Fernández, E., P. Boyd, P. M. Holligan, and D. S. Harbour (1993), Production of organic and inorganic carbon within a large scale coccolithophore bloom in the northeast Atlantic Ocean, *Mar. Ecol. Prog. Ser.*, *97*, 271–285.

Francois, R., S. Honjo, R. Krishfield, and S. Manganini (2002), Factors controlling the flux of organic carbon to the bathypelagic zone of the ocean, *Global Biogeochem. Cycles*, *16*(4), 1087, doi:10.1029/2001GB001722.

Fukushima, H., and J. Ishizaka (1993), Special features and applications of CZCS data in Asian waters, in *Ocean Colour: Theory and Applications in a Decade of CZCS Experience*, edited by P. Schlittenhardt and V. Barale, pp. 213–236, Elsevier, New York.

Garcia-Soto, C., E. Fernandez, R. D. Pinigree, and D. S. Harbour (1995), Evolution and structure of a shelf coccolithophore bloom in the western English Channel, *J. Plankton Res.*, *17*, 2011–2036.

Gayoso, A. M. (1995), Bloom of Emiliania huxleyi (Prymnesiophyceae) in the western South Atlantic Ocean, *J. Plankton Res.*, *17*, 1717–1722.

Geider, R. J. (1987), Light and temperature dependence of the carbon to chlorophyll a ratio in microalgae and cyanobacteria: Implications for physiology and growth of phytoplankton, *New Phytol.*, *106*, 1–34.

Gordon, H. R. (1997), Atmospheric correction of ocean color imagery in the Earth Observing System era, *J. Geophys. Res.*, *102*, 17,081–17,106.
Gordon, H. R., and T. Du (2001), Light scattering by nonspherical particles: Application to coccoliths detached from *Emiliania huxleyi*, *Limnol. Oceanogr.*, *46*, 1438–1454.
Gordon, H. R., and W. R. McCluney (1975), Estimation of the depth of sunlight penetration in the sea for remote sensing, *Appl. Opt.*, *14*, 413–416.
Gordon, H. R., and A. Y. Morel (1983), *Remote Assessment of Ocean Color for Interpretation of Satellite Visible Imagery: A Review*, 114 pp., Springer, New York.
Gordon, H. R., and M. Wang (1994), Retrieval of water-leaving radiance and aerosol optical thickness over the oceans with SeaWiFS: A preliminary algorithm, *Appl. Opt.*, *33*, 443–452.
Gordon, H. R., O. B. Brown, R. H. Evans, J. W. Brown, R. C. Smith, K. S. Baker, and D. K. Clark (1988), A semi-analytic radiance model of ocean color, *J. Geophys. Res.*, *93*, 10,909–10,924.
GREPMA (1981), Satellite (AVHRR/NOAA-9) and ship studies of a coccolithophorid bloom in the western English Channel, *Mar. Nature*, *1*, 1–14.
Head, R. N., D. W. Crawford, J. Egge, D. Lesley, S. Kristiansen, E. Maranon, D. Pond, D. A. Purdie, and R. P. Harris (1998), The hydrography and biology of a bloom of the coccolithophorid *Emiliania huxleyi* in the northern North Sea, *J. Sea Res.*, *39*, 255–266.
Holligan, P. M., M. Viollier, D. S. Harbout, P. Camus, and M. Champagne-Philippe (1983), Satellite and ship studies of coccolithophore production along a continental shelf edge, *Nature*, *304*, 339–342.
Holligan, P. M., et al. (1993), A biogeochemical study of the coccolithophore, *Emiliania huxleyi*, in the North Atlantic, *Global Biogeochem. Cycles*, *7*, 879–900.
Iglesias-Rodrigues, D., R. Armstrong, R. Feely, R. Hood, and J. Kleypas (2001), SMP Workshop assesses role of calcification in ocean carbon cycle, *U.S. JGOFS Newsl.*, *11*(3), 9–10.
Kai, M., T. Hara, H. Aoyama, and N. Kuroda (1999), A massive coccolithophorid bloom observed in Mikawa Bay, Japan, *J. Oceanogr.*, *55*, 395–406.
Keller, M. D., W. K. Bellows, and R. R. L. Guillard (1989), Dimethyl sulfide production in marine phytoplankton, in *Biogenic Sulfur in the Environment*, edited by E. S. Saltzman and W. J. Cooper, pp. 167–182, Am. Chem. Soc., Washington, D. C.
Keller, M. D., D. W. Townsend, S. G. Ackleson, P. M. Holligan, W. M. Balch, and P. A. Matrai (1992), Observations of coccolithophore blooms in the Gulf of Maine, in *Gulf of Maine Scientific Workshop*, edited by J. Wiggin and C. Mooers, pp. 259–263, Univ. of Mass. Urban Harbors Inst., Boston.
Lavrentyev, P. J., D. A. Stockwell, and T. E. Whitledge (2001), The distribution of microbial plankton in the Bering Sea during the anomalous coccolithophore bloom in summer 1998 (abstract), in *2001 Aquatic Sciences Meeting*, edited by J. D. Ackerman and S. Twombly, p. 86, Am. Soc. of Limnol. and Oceanogr., Albuquerque, N. M.
Longhurst, A. R. (1998), *Ecological Geography of the Sea*, Elsevier, New York.
Maier-Reimer, E. (1996), Dynamic vs. apparent Redfield radio in the oceans: A case for 3D models, *J. Mar. Syst.*, *9*, 113–120.
Malin, G., S. Turner, P. Liss, P. Holligan, and D. Harbour (1993), Dimethylsulphide and dimethylsulphoniopropianate in the northeast Atlantic during the summer coccolithophore bloom, *Deep Sea Res., Part I*, *40*, 1487–1508.
Matrai, P. A., and M. D. Keller (1993), Dimethylsulfide in a large-scale coccolithophore bloom in the Gulf of Maine, *Cont. Shelf Res.*, *13*, 831–843.
Milliman, J. D. (1993), Production and accumulation of calcium carbonate in the ocean: Budget of a nonsteady state, *Global Biogeochem. Cycles*, *7*, 927–957.
Milliman, J., P. J. Troy, W. Balch, A. K. Adams, Y.-H. Li, and F. T. MacKenzie (1999), Biologically-mediated dissolution of calcium carbonate above the chemical lysocline?, *Deep Sea Res., Part I*, *46*, 1653–1669.
Morel, A. (1988), Optical modeling of the upper ocean in relation to its biogenous matter content (case 1 waters), *J. Geophys. Res.*, *93*, 10,749–10,768.
Morse, J. W., and F. T. Mackenzie (1990), *Geochemistry of Sementary Carbonates*, Elsevier, New York.
Mueller, J. L., et al. (2003), *Ocean Optics Protocols for Satellite Ocean Color Sensor Validation*, vol. 3, *Radiometric Measurements and Data Analysis Protocols*, rev. 4, 78 pp., NASA Goddard Space Flight Cent., Greenbelt, Md.
Najjar, R. G., J. L. Sarmiento, and J. R. Toggweiler (1992), Downward transport and fate of organic matter in the ocean: Simulations with a general circulation model, *Global Biogeochem. Cycles*, *6*, 45–76.
Napp, J. M., and G. L. J. Hunt (2001), Anomalous conditions in the southeastern Bering Sea 1997: Linkages among climate, weather, ocean and biology, *Fish. Oceanogr.*, *10*, 61–68.
Paasche, E. (1962), Coccolith formation, *Nature*, *193*, 1094–1095.
Paasche, E. (1998), Roles of nitrogen and phosphorus in coccolith formation in *Emiliania huxleyi* (Prymnesiophyceae), *Eur. J. Phycol.*, *33*, 33–42.
Paasche, E. (1999), Reduced coccolith calcite production under light-limited growth: A comparative study of three clones of *Emiliania huxleyi* (Prymnesiophyceae), *Phycologia*, *38*, 508–516.
Paasche, E. (2002), A review of the coccolithphorid *Emiliania huxleyi* (Prymnesiophyceae), with particular reference to growth, coccolith formation, and calcification-photosynthesis interactions, *Phycologia*, *40*, 503–529.
Paasche, E., S. Brubak, S. Skattebøl, J. R. Young, and J. C. Green (1996), Growth and calcification in the coccolithophorid *Emiliania huxleyi* (Haptophyceae) at low salinities, *Phycologia*, *35*, 394–403.
Peng, T.-H., R. Wanninkhof, J. L. Bullister, R. A. Feely, and T. Takahashi (1998), Quantification of decadal anthropogenic CO_2 uptake in the ocean based on dissolved inorganic carbon measurements, *Nature*, *396*, 560–563.
Riebesell, U., D. A. Wolf-Gladrow, and V. Smetacek (1993), Carbon dioxide limitation of marine phytoplankton growth rates, *Nature*, *361*, 249–251.
Riebesell, U., I. Zondervan, B. Rost, P. D. Tortell, R. E. Zeebe, and F. M. M. Morel (2000), Reduced calcification of marine plankton in response to increased atmospheric CO_2, *Nature*, *407*, 311–313.
Riebesell, U., I. Zondervan, B. Rost, and R. E. Zeebe (2001), Effects of increasing atmospheric CO_2 on phytoplankton communities and the biological carbon pump, *Global Change Newsl.*, *47*, 12–15.
Robertson, J. E., C. Robinson, D. R. Turner, P. Holligan, A. J. Watson, P. Boyd, E. Fernandez, and M. Finch (1994), The impact of a coccolithophore bloom on oceanic carbon uptake in the northeast Atlantic during summer 1991, *Deep Sea Res., Part I*, *41*, 297–314.
Sabine, C. L., et al. (2004), The oceanic sink for anthropogenic CO_2, *Science*, *305*, 367–371.
Samtleben, C., and T. Bickert (1990), Coccoliths in sediment traps from the Norwegian Sea, *Mar. Micropaleontol.*, *16*, 39–64.
Sarmiento, J. L., J. Dunne, A. Gnanadesikan, R. M. Key, K. Matsumoto, and R. Slater (2002), A new estimate of the $CaCO_3$ to organic carbon export ratio, *Global Biogeochem. Cycles*, *16*(4), 1107, doi:10.1029/2002GB001919.
Seibold, E., and W. H. Berger (1982), *The Sea Floor: An Introduction to Marine Geology*, 288 pp., Springer, New York.
Shaw, G. E. (1983), Bio-controlled thermostasis involving the sulfur cycle, *Clim. Change*, *5*, 297–303.
Steele, J. H., and I. E. Baird (1962), Further relations between primary production, chlorophyll and particulate carbon, *Limnol. Oceanogr.*, *7*, 42–47.
Stockwell, D. A., T. E. Whitledge, T. Rho, P. J. Stabeno, K. O. Coyle, J. M. Napp, S. I. Zeeman, and G. L. Hunt (2000), Field observations in the southeastern Bering Sea during three years with extensive coccolithophorid blooms (abstract), *Eos Trans. AGU*, *81*, Ocean Sci. Meet. Suppl., Abstract OS12D-03.
Stumm, W., and J. J. Morgan (1981), *Aquatic Chemistry*, John Wiley, Hoboken, N. J.
Sundquist, E. T. (1993), The global carbon dioxide budget, *Science*, *259*, 934–941.
Takahashi, W., T. Hiwatari, H. Fukushima, M. Toratani, and T. Akano (1995), High-reflectance waters of possible coccolithophore blooms in NW pacific: Analysis of 1979–86 Nimbus-7/CZCS data set, *Japanese*, *6*, 477–486.
Townsend, D. W., M. D. Keller, P. M. Holligan, S. G. Ackleson, and W. M. Balch (1994), Blooms of the coccolithophore *Emiliania huxleyi* with respect to hydrography in the Gulf of Maine, *Cont. Shelf Res.*, *14*, 979–1000.
Troy, P. J., Y.-H. Li, and F. T. MacKenzie (1997), Changes in surface morphology of calicite exposed to the oceanic water column, *Aquat. Geochem.*, *3*, 1–20.
Tyrell, T., P. M. Holligan, and C. D. Mobley (1999), Optical impacts of oceanic coccolithophore blooms, *J. Geophys. Res.*, *104*, 3223–3241.
Van der Wal, P., R. S. Kempers, and M. J. W. Veldhuis (1995), Production and downward flux of organic matter and calcite in a North Sea bloom of the coccolithophore *Emiliania huxleyi*, *Mar. Ecol. Prog. Ser.*, *126*, 247–265.
Volk, T., and M. I. Hoffert (1985), Ocean carbon pumps: Analysis of relative strengths and efficiencies in ocean-driven atmospheric pCO_2 changes, in *The Carbon Cycle and Atmospheric CO_2: Natural Varia-*

tions Archean to Present, *Geophys. Monogr. Ser.*, vol. 32, edited by E. T. Sundquist and W. S. Broecker, pp. 99–110, AGU, Washington, D. C.

Wal, P. D., R. S. Kempers, and M. J. W. Veldhuis (1995), Production and downward flux of organic matter and calcite in a North Sea bloom of the coccolithophore *Emiliania huxleyi*, *Marine Ecol. Prog. Ser.*, *126*, 247–265.

Wollast, R. (1994), The relative importance of biomineralization and dissolution of $CaCO_3$ in the global carbon cycle, report, edited by F. Doumenge, D. Allemand, and A. Toulemont, pp. 13–35, Mus. Oceanogr., Monaco.

Young, J. R., and P. Ziveri (1999), Calculation of coccolith volume and its use in calibration of carbonate flux estimates, *Deep Sea Res., Part II*, *47*, 1679–1700.

W. M. Balch, E. S. Booth, B. C. Bowler, and D. T. Drapeau, Bigelow Laboratory for Ocean Sciences, P.O. Box 475, West Boothbay Harbor, ME 04575, USA. (bbalch@bigelow.org; ebooth@bigelow.org; bbowler@bigelow.org; ddrapeau@bigelow.org)

H. R. Gordon, Physics Department, University of Miami, Coral Gables, FL 33124, USA. (gordon@phyvax.ir.miami.edu)

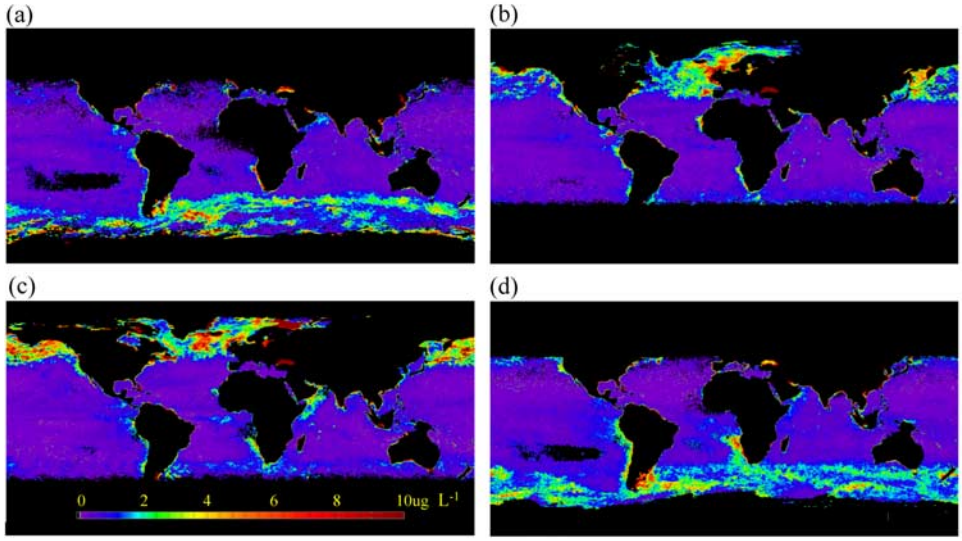

Figure 5. Global composite images of suspended PIC concentration calculated from MODIS/Terra data using two-band calcite algorithm. See text for other details of how the data were processed. The color scale is highlighted in Figure 5c. These data were binned into 36 km and 90 day averages, and thus the standard error will be <0.08 μgPIC L^{-1} (see Table 2), well below the average seawater concentration of ~2 μgPIC L^{-1}. (a) January–March. (b) April–June. (c) July–September. (d) October–December.